ACTINIDE RESEARCH QUARTERLY

Second Quarter 2018

Seaborg Institute Postdocs

Bringing new ideas to long-standing challenges in transactinium science

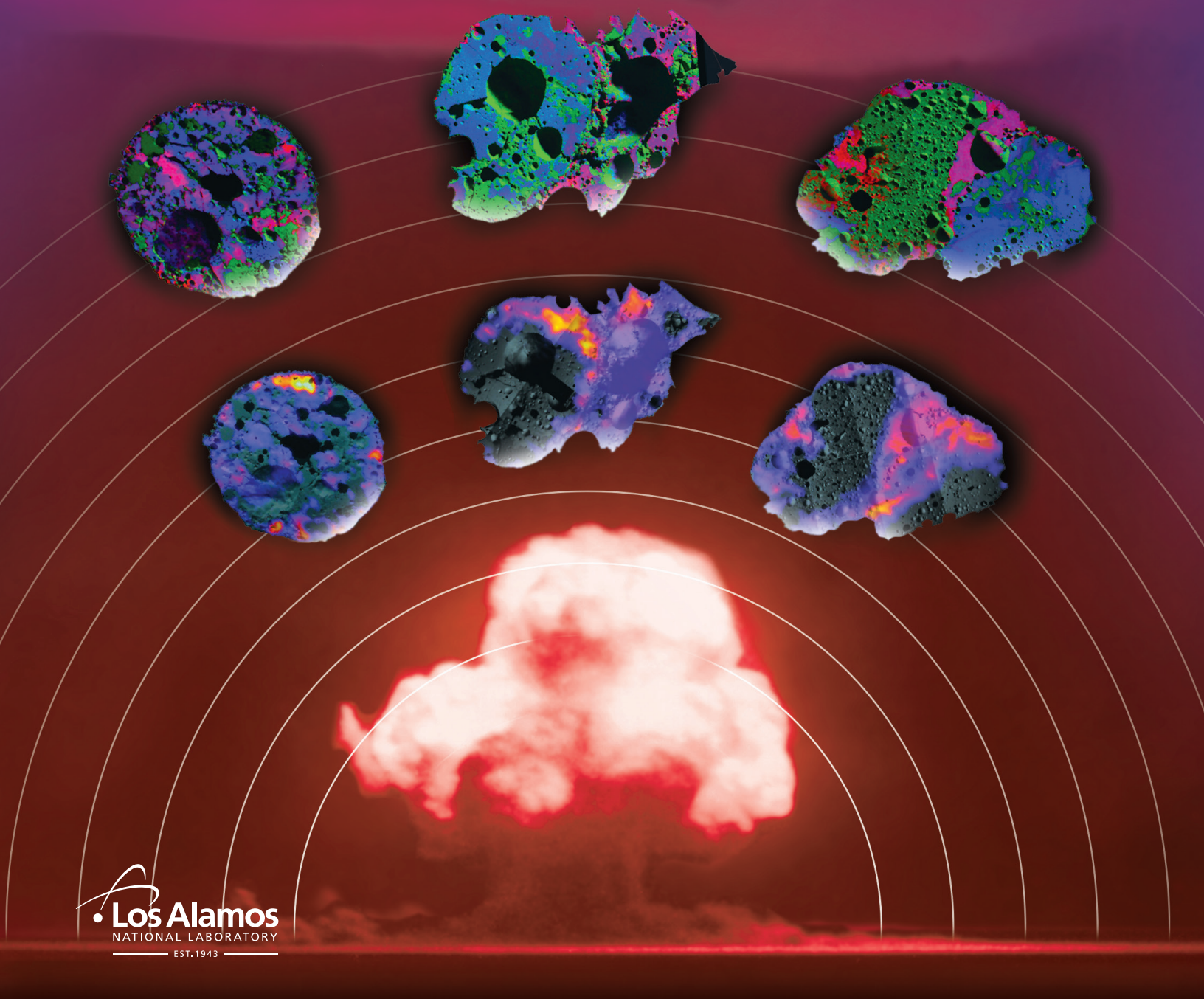

Los Alamos NATIONAL LABORATORY EST. 1943

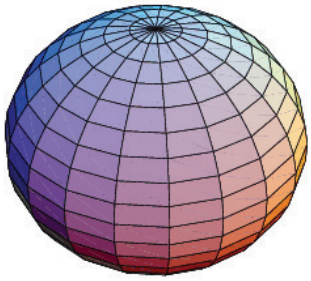

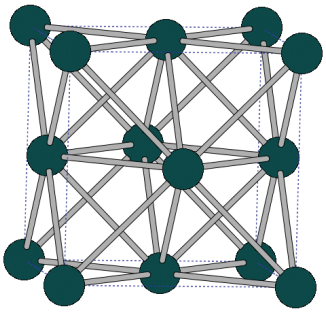

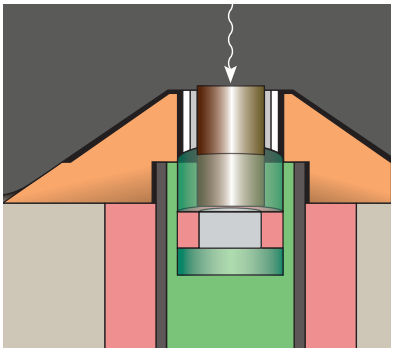

Preface

In this quarter, we present research from nine recent Seaborg postdoctoral fellows, many of whom have continued their work at Los Alamos National Laboratory as scientists.

This issue focuses on challenges in actinide science relating to materials, isotope detection, and nuclear forensics. Detecting and tracking nuclear materials through their physical signatures is vital for national security and operational safety, and several fellows have worked to tackle these issues. McIntosh (*p7*) has used a new analytical tool to successfully detect plutonium in fuel and soil samples, crucially demonstrating its versatility and nondestructive functionality. Campbell (*p16*) has also applied another nondestructive spectroscopic method for the detection of isotopes in uranium ores and simulated used nuclear fuels which is rapid and field-deployable. Malone discusses on *p24* the undeveloped potential for magnetic resonance to revolutionize this field with advanced imaging techniques suitable for actinides. On *p35*, Barker outlines a fundamental approach to improving the detection of actinide ions using photoluminescence, showing considerable increases in efficiency. Nuclear forensics work by Bonamici (*p2*) on the historical Trinity explosion (featured on our front cover) is highlighted opposite.

Plutonium is well known for its unique characteristics that make it challenging to work with and difficult to predict how it ages (for instance, in the nation's nuclear stockpile) but keep scientists fascinated. For instance, the metal becomes denser when it is heated, and the constant emission of alpha particles from radioactive decay causes the element to self-heat and damages its crystal structure. Marchi describes on *p29* several approaches for overcoming issues caused by self-heating to obtain more accurate density measurements for Pu, which can inform structural changes related to aging. Meanwhile, Olive (*p39*) has used spectroscopic methods to examine the mechanism of structural damage caused by self-irradiation. In another approach to examine actinide structure and properties, Jacobsen (*p12*) describes the design of the first and, currently, only experimental capacity for probing radioactive elements under pressure.

Much of this work uses theoretical calculations to help interpret data and verify conclusions. On *p20*, Ellis shows that a purely theoretical approach can be used to lead the way and guide experiments to find the lowest-lying nuclear transition in ^{229}Th, a much sought-after result which could lead to the development of a "nuclear clock".

These articles showcase the problems being addressed by the future generation of scientists, and the fresh ideas they are bringing to old challenges.

— Owen Summerscales | Editor

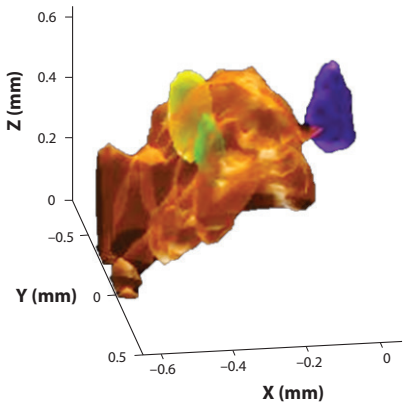

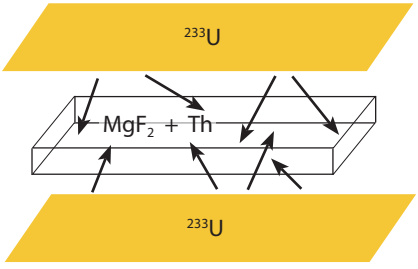

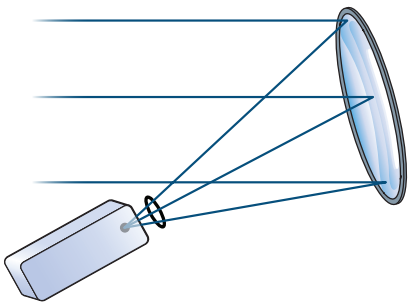

In this issue

About the cover: *The fireball from the Trinity explosion (July 16, 1945) produced glassy fallout debris containing a signature of its unique characteristics.* Bonamici *(p2) analyzed these airborne particles to produce phase maps indicating elemental distribution and radioactive maps showing the distribution of radionuclides. This type of nuclear forensics work aims to develop tools to identify unattributed nuclear explosions and identify future threats.*

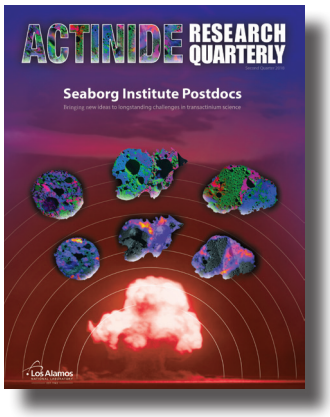

Volatility in the Trinity Fireball as Recorded in Glassy Fallout Debris **2**
Chloë Bonamici

Plutonium Characterization in Spent Nuclear Fuel and Contaminated Soil Using a New, Nondestructive Analytical Tool **7**
Kathryn McIntosh

Moving Actinide Science to New Extremes (of Pressure) **12**
Matthew Jacobsen

A Promising Tool for Nuclear Safeguards: Laser-Induced Breakdown Spectroscopy **16**
Keri Campbell

Towards a Nuclear Clock: Theoretical Studies of Thorium Materials for the Direct Measurement of the Lowest-Lying Nuclear Transition in ^{229}Th **20**
Jason Ellis

Magnetic Resonance for Actinide Science: A Perspective **24**
Michael Malone

Toward High-Precision Plutonium Density Measurements: Investigating Errors in Measuring Self-Heating Samples **29**
Alexandria Marchi

Actinide Detection Using Photoluminescence: Resonant Non-Radiative Energy Transfer Between Actinyl Ions **35**
Beau J. Barker

Radiation Damage in Plutonium from a Local Structure Perspective **39**
Daniel T. Olive

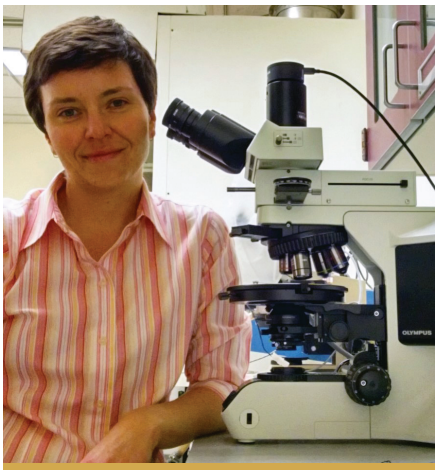

Chloë Bonamici

Chloë Bonamici was a Seaborg postdoc from 2014 to 2015 under the mentorship of William Kinman. She is now an assistant professor in Earth and Environmental Sciences at New Mexico Tech.

Volatility in the Trinity Fireball as Recorded in Glassy Fallout Debris

Chemical and isotopic analysis of glassy fallout debris from a nuclear explosion is a powerful forensic tool for identifying nuclear devices and preventing future nuclear attacks. It has, however, long been recognized that the composition of glassy fallout debris does not directly reflect the nature of the originating device. Physical, chemical, and nuclear processes within the fireball lead to the preferential segregation of elements and isotopes—i.e., fractionation—into different regions of the fallout, which hinders forensic reconstruction of the device. In order to retrieve as much information as possible about the device composition, it is necessary to identify the processes occurring in the fireball and account for the systematic fractionating effects of these processes.

Using minimally-destructive analysis to observe microscale variations

In order to study processes occurring within the fireball, we selected aerodynamic beads of glassy fallout (Fig. 1) from the first nuclear test, Trinity (July 16, 1945, New Mexico). Vesicular (cavity-rich), amorphous crusts of glassy "trinitite" are widely available for research by both federal and nonfederal entities; however, these ground-crust samples were avoided in the present study because it is still unknown to what extent they formed in place by melting of the ground surface versus in the fireball. The beads clearly formed within the fireball and solidified before falling out, and therefore unambiguously retain information about fireball processes.

Recent studies of trinitite have shown that the debris is extremely heterogeneous at the microscopic scale (Fig. 1). Therefore, analytical methods for studying trinitite composition that involve bulk dissolution necessarily result in averaging of the data derived from the debris. Because this microscale variation is important for understanding the formation of the debris, we have characterized the trinitite beads using several non-destructive or minimally-destructive techniques that allow for in situ determination of the chemical and isotopic composition of regions of the glass ~10–40 μm in diameter. Data presented here were acquired using a combination of scanning electron microscopy (SEM), energy-dispersive X-ray spectroscopy (EDS), digital autoradiography, electron microprobe analysis (EMPA), and secondary ion mass spectrometry (SIMS).

Our study focused on identifying fine-scale variations in both the major- and trace-element chemistry of the trinitite beads in order to better understand the transformation of material into glassy fallout. The major-element composition of debris (elements making up ≥ 1 wt.%) was determined by the ground material incorporated into the fireball. The trace-element composition (elements making up ≤ 0.1 wt.%, or ~1000 ppm) meanwhile was determined by a combination of trace elements within the ground material and dispersed device and detonation structure (tower) material.

Composition of fallout debris

Phase maps (Fig. 1) and EMPA data show that the trinitite beads studied are composed of three distinctly different types of glass: an essentially pure silica glass, a glass rich in alkali elements K and Na, and a glass characteristically containing Ca,

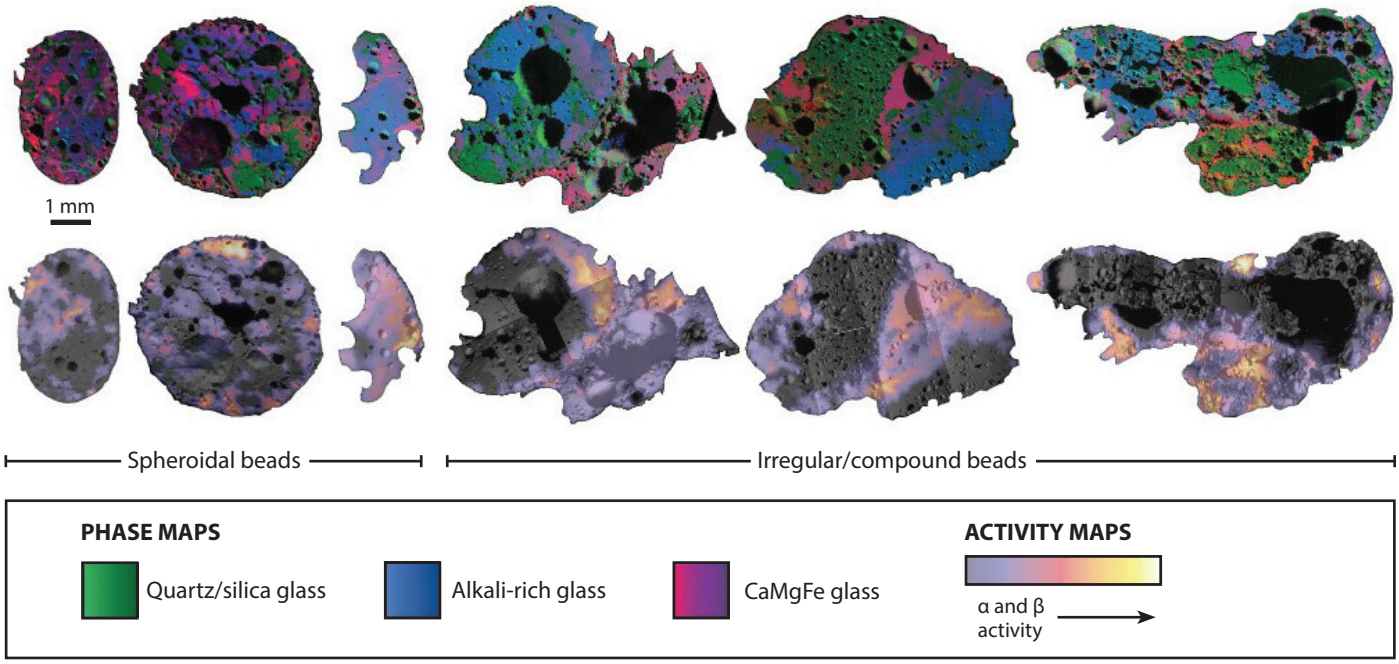

Mg, and Fe. The silica and alkali glasses have compositions that are directly equivalent to mineral constituents in the test-site sand, as would be expected for glasses formed by melting individual sand grains. However, the compositional variations within the CaMgFe glass are large and complex.

In order to understand the chemical relationship of the CaMgFe glass to the test-site sand, we normalized the measured CaMgFe glass compositions to the estimated average bulk composition of the test-site sand (Fig. 2). Thermodynamic calculations, experiments, and studies of natural magmatic rocks show that melting of a quartzofeldspathic starting-material (like the Trinity test-site sand) will produce glasses enriched in elements such as Na, K, and Si, but depleted in elements like Ca, Mg, and Fe. The patterns of elemental enrichment and depletion in the CaMgFe glass are therefore not consistent with melting. Instead, the element variation patterns, which can range from highly enriched to quite depleted (Fig. 3), are more consistent with those expected for a melt formed by condensation from a vapor. We conclude that the elemental variation in CaMgFe glass arises from characteristic differences in condensation temperature (volatility) of different elements. In other words, the CaMgFe glass is chemically distinct because it formed by condensation from a vapor, not by melting of a solid.

Digital autoradiography is a technique that images radioactivity similar to the way photographic film images light; in this context, it can identify radioactive constituents that derive from the originating device. We found that these autoradiography maps of trinitite beads (Fig. 1) show no activity in unmelted mineral fragments, silica glass, or alkali glass. Debris components formed through simple melting of ground material are therefore unlikely to retain detectable chemical or isotopic information about a device. Detectable radioactivity occurs only in the condensation-formed CaMgFe glass, and thus we conclude that only liquids (and, subsequently, glasses) formed in this manner contain significant quantities of radioactive, device-derived constituents. Consequently, CaMgFe glass is the primary repository for compositional signals from the nuclear device.

Figure 1. Two types of images of six samples of aerodynamic trinitite beads analyzed for this study, showing their heterogeneous nature. Phase maps (top row) show the different types of trinitite glass determined from element concentrations, generated by mapping major element concentrations with SEM-EDS (scanning electron microscopy, energy-dispersive X-ray spectroscopy) and color-coded based on their relative abundance. The radioactivity maps (bottom row) show the distribution of radionuclides; the legend provides a radioactivity scale (dark gray indicates no radioactivity); maps were determined using autoradiography.

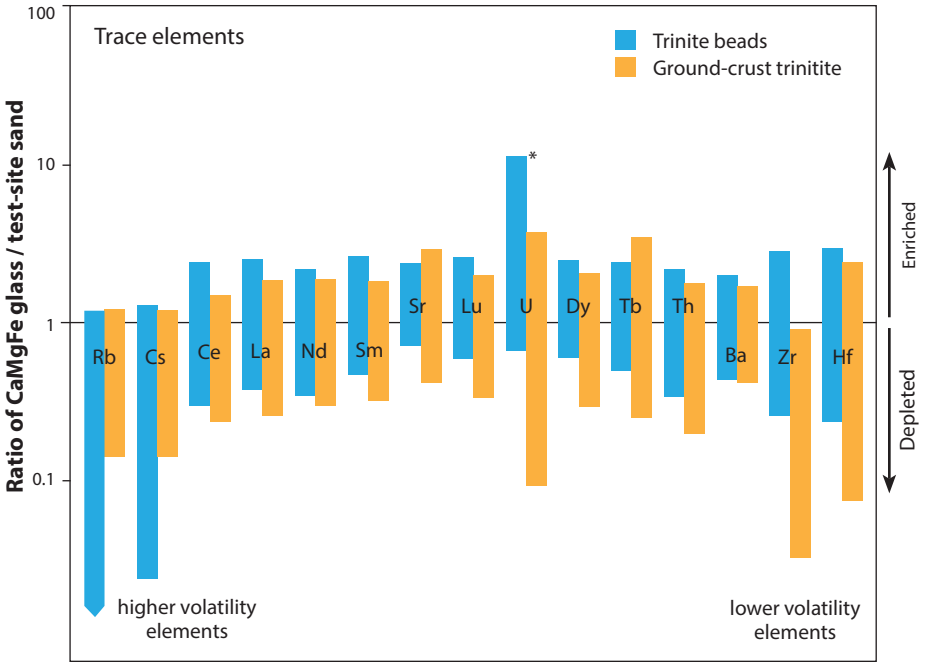

Figure 2. Bar plot showing how trace element concentrations vary in trinitite CaMgFe glass. Trace elements were measured by SIMS (secondary ion mass spectrometry); the top of each bar is the maximum concentration measured and the bottom is the minimum concentration measured. Every trace element shows a large range of concentrations in the CaMgFe glass (note logarithmic scale), consistent with formation by condensation from a vapor. Elements in a glass formed by melting would show a generally smaller range of concentrations and a more systematic pattern of depletion or enrichment. Trace element abundance in CaMgFe glass is normalized to the average sand composition of the Trinity test site. * The highlighted bar shows that there is more U in aerodynamic trinitite than in ground-crust trinitite.

Because ground-crust trinitite has been shown to have significant compositional signal from the device, it is probable that much of the ground crust is made up of CaMgFe glass that, like glasses of the aerodynamic beads, formed initially by condensation within the cloud. However, whereas the melt composing the beads formed high enough in the cloud to solidify before reaching the ground, the melt that constituted the ground-crust material must have formed lower in the cloud, splashing to the ground while still molten.

Volatility of glasses

Recent work has shown that as much as 50–60 vol.% of the glass within Trinity fallout formed as liquid condensed from the fireball plasma (i.e., the CaMgFe glass) as opposed to melting of local sediment. Thus, both the major-element and the radionuclide compositions of certain glasses are controlled by chemical volatility. Variations in the major-element compositions can be used to locate the different glass components in "volatility space", as shown in Fig. 3. In this figure, we compare the relative proportions of low-, intermediate-, and high-volatility major elements from each location measured in the trinitite glass. Silica and alkali glass compositions show limited ranges of volatility; however, the condensation-formed CaMgFe glass shows a very large range in volatility, with compositions extending almost continuously from a very low volatility endmember, containing large quantities of Ca and Al, toward intermediate- and high-volatility compositions. Assuming that melts enriched in low-volatility elements condensed first, and that condensates became progressively enriched in intermediate- and high-volatility elements with time, the observed volatility trend in CaMgFe glass provides a timeline of condensation (Fig. 3).

The near-linearity of the CaMgFe glass major-element volatility trend allows for the formulation of a simple volatility index. By plotting trace element abundance as a function of the volatility index, we assessed the timing of the incorporation of trace elements into fallout glass. As might be expected, the abundance of high-volatility trace elements, such as Rb and Cs, increases with increasing volatility index. Conversely, low-volatility trace element abundance decreases with increasing volatility index. These patterns confirm the inference based on autoradiography

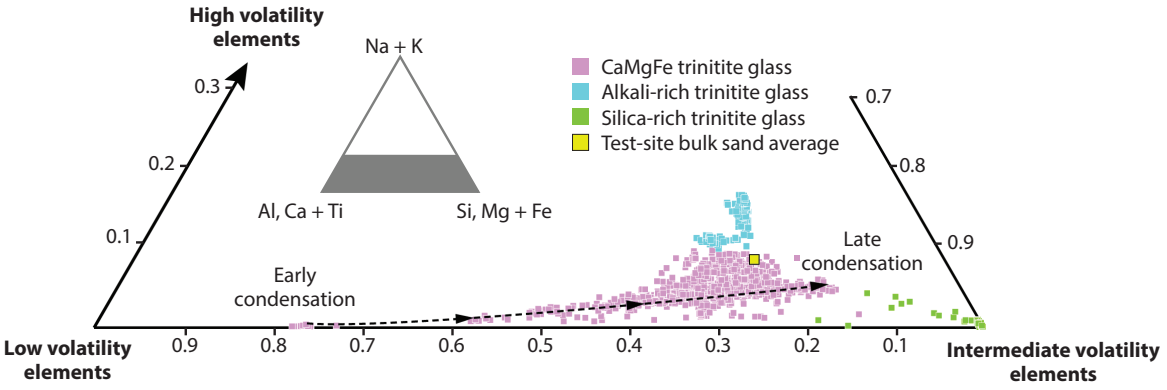

(Fig. 1) that trace elements, including radioisotopes originating from the nuclear device, are incorporated into fallout glass by volatility-controlled co-condensation of vaporized ground and device material.

Actinide fractionation

The fractionation of actinides and their isotopes during fallout formation can also be assessed using this volatility index, which shows the compositional changes in the fireball with time and decreasing temperature. The Trinity device contained both Pu and natural U, and minerals in the test-site sand contain abundant natural U. The $^{239}Pu/^{238}U$ ratios measured in trinitite beads decrease with increasing volatility index (Fig. 4a), indicating that Pu was less volatile than U within the fireball. While this relationship has been previously suggested, this is the first study to demonstrate it. This was achieved using an independent volatility scale based on stable element measurements. In contrast, the $^{235}U/^{238}U$ ratio remains the same over the entire volatility index range and, within analytical error, identical to the original, natural isotopic composition of both the device and sand uranium (Fig. 4b). Thus, while the elements Pu and U were fractionated from each other in the Trinity fireball, the isotopes of U were not.

Uranium fractionation can be further understood by comparing data from the aerodynamic trinitite beads with ground-crust trinitite. The data shown in Fig. 2 suggest that, on average, U is more abundant in aerodynamic trinitite than in the original test-site sand or in the ground-crust trinitite. Our data demonstrate that aerodynamic trinitite was generally enriched in U at all times and over all volatility conditions, relative to ground-crust trinitite. We conclude that melts that condensed close enough to the ground surface to be rained out while still molten and form the ground crust contain less device-derived U than melts that condensed (and solidified) higher within the fireball to form the beads. Thus, U was likely less abundant in regions of the fireball closer to the ground.

Summary

Microanalysis of aerodynamic glassy fallout from the Trinity test suggests that some of the fallout glasses were formed by melting individual sand grains, but that much of the melt condensed from vaporized sediment (forming a glass characteristically containing Ca, Mg, and Fe). As would be expected, the order of condensation of both major and trace elements was determined by elemental volatility within the fireball. The major-element composition of a glass can be used to calculate a volatility index, which provides a volatility scale for trace elements, including those derived from the device. This volatility index can be used to show that Pu was less volatile than U in the fireball, that U isotopes were not fractionated during the explosion, and that U was more abundant higher in the fireball than near the ground surface.

Figure 3. Trinitite glass compositions plotted in major-element "volatility space", a triangular compositional space where the three corners of the triangle represent high-volatility (Na, K), low-volatility (Al, Ca, Ti) and intermediate-volatility (Si, Mg, Fe) elements. The inset small gray triangle shows the whole "volatility space" and the shaded region shows where the trinitite data (expanded below) plot. The numbers along the triangle edges represent what fraction of the glass is made up of the high-, low-, or intermediate-volatility elements. The black dashed line highlights the compositional trend of the CaMgFe glass, which extends from a region enriched in low-volatility elements to a region enriched in high-volatility elements. This compositional trend also reflects a temporal trend, showing early to late condensation within the nuclear fireball.

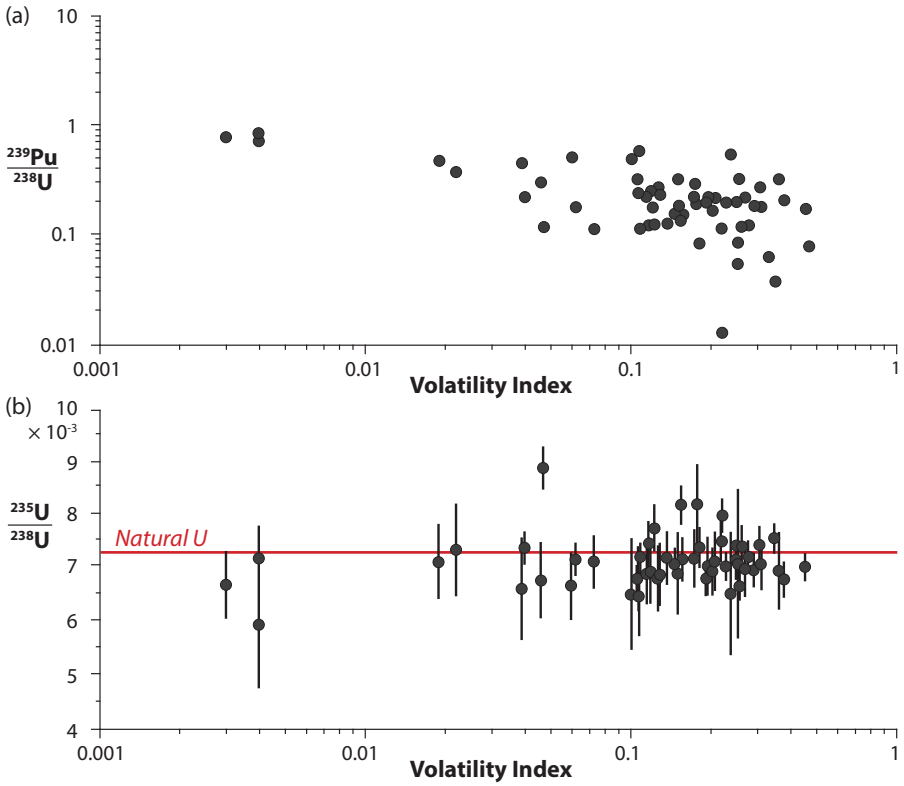

Figure 4. Plots showing actinide isotope trends in the condensation-formed CaMgFe trinitite glass: **(a)** Ratio of the most abundant Pu and U isotopes in trinitite glass plotted as function of major-element volatility index (Na + K/Al + Ca + Ti). This plot shows high Pu/U in early condensate glasses decreasing to lower Pu/U in later condensate glasses, suggesting that U behaved as a higher volatility element than Pu in the fireball. **(b)** $^{235}U/^{238}U$ in trinitite as a function of volatility index. This plot shows that the original natural U isotope composition of the Trinity tamper was not changed during the explosion, therefore isotopes of U were not fractionated in the nuclear fireball.

Altogether, these findings demonstrate that microanalytical techniques can provide valuable information about how glassy fallout debris forms and how it records the chemical and isotopic composition of a nuclear device. This is a vital step in the forensic reconstruction of a nuclear explosion.

Acknowledgments

The author thanks Warren Oldham and Susan Hanson for trinitite bead samples; John Fournell and Richard Hervig for assistance with microanalysis data collection; Mindy Zimmer and Anthony Pollington for helpful discussions. This work was supported through the Glenn T. Seaborg Institute for Actinide Science, the Strategic Outcomes Office of LANL, and the US DOE National Nuclear Security Administration.

Further reading:

1. *E. C. Freiling, "Radionuclide fractionation in bomb debris", Science 1961, 133, 1991–1998.*
2. *G. N. Eby, N. Charnley, D. Pirrie, R. Hermes, J. Smoliga, and G. Rollinson, "Trinitite redux: Mineralogy and petrology", Am. Mineral. 2015, 100, 427–441.*
3. *R. E. Hermes and W. B. Strickfaden, "A new look at trinitite", Nuclear Weapons Journal 2005, 2, 2–7.*
4. *F. Belloni, J. Himbert, O. Marzocchi, and V. Romanello, "Investigating incorporation and distribution of radionuclides in trinitite" J. Environ. Radioact. 2011, 102, 852–862.*
5. *D. K. Smith and R. W. Williams, "The dynamic movement of plutonium in an underground nuclear test with implications for the contamination of groundwater", J. Radioanal. Nucl. Chem. 2005, 263, 2, 281–285.*
6. *J. J. Bellucci, A. Simonetti, E. C. Koeman, C. Wallace, and P. C. Burns, "A detailed geochemical investigation of post-nuclear detonation trinitite glass at high spatial resolution: Delineating anthropogenic vs. natural components", Chem. Geol. 2014, 365, 69–86.*
7. *C. E. Bonamici, R. L. Hervig, and W. S. Kinman, "Tracking radionuclide fractionation in the first atomic explosion using stable elements", Anal. Chem. 2017, 89, 9877–9883.*

Plutonium Characterization in Spent Nuclear Fuel and Contaminated Soil Using a New, Nondestructive Analytical Tool

Kathryn McIntosh

Kathryn McIntosh was a Seaborg Institute postdoc under the mentorship of George Havrilla from 2013 to 2015 and is now a staff member in Chemical Diagnostics and Engineering (C-CDE). One of her areas of interest is instrument and method development for nondestructive detection and characterization of actinides.

No single analytical technique can be relied upon to provide all the information desired for a sample. In elemental analysis, questions to be answered include: What elements are present? Where are they located? In what quantities? Characterization capabilities to reliably answer these and other questions are of vital importance to Los Alamos National Laboratory's (LANL's) national security mission.

In our laboratory, we have utilized X-ray fluorescence spectrometry (XRF) techniques for the characterization of a wide variety of sample types. The principle of XRF is that when atoms in a sample are excited by a source of sufficient energy (in this case, X-rays generated by an X-ray tube) they emit photons with characteristic energies that result from transitions between electronic orbitals. The energies (or wavelengths) of the emitted fluorescent X-rays identify what elements are present, while the intensity of the X-rays is proportional to the concentration of each element.

The primary advantage of XRF over other elemental analysis techniques is that it is nondestructive. Other benefits include direct measurements with minimal sample preparation, rapid analysis, and applicability over a wide range of elements (typically Na–Pu) and concentrations. This article highlights the development of unique capabilities in actinide characterization, demonstrated by an analysis of two challenging sample types.

Spent nuclear fuel analysis

The measurement of Pu in spent nuclear fuel is important for material control and accountancy in reprocessing streams for monitoring plant processes and preventing undetected diversion. While a variety of routine methods are available for Pu determination, including coulometry, alpha spectrometry, and isotope dilution mass spectrometry (IDMS), these each have limitations primarily related to speed of analysis due to extensive sample preparation (e.g., spiking, column separations, and dilution) or long counting times, both of which can span hours to days.

High-resolution X-ray spectrometry (hiRX) is a new analytical approach for the rapid determination of Pu in spent fuel that we expect will offer accurate analysis with reduced sample handling and waste. It is based on Monochromatic Wavelength Dispersive X-Ray Fluorescence (MWDXRF), which has existed commercially for the last 15 years, although small in scope. Currently, it has been applied initially to sulfur analysis in petroleum by X-ray Optical Systems (XOS)—we have worked with this company to develop hiRX, which is specifically aimed at Pu determination.

We recently demonstrated the first determination of Pu in actual spent nuclear fuel using hiRX. This instrument utilizes doubly-curved crystal (DCC) optics as the key innovation of MWDXRF to achieve sensitive and selective detection (breadboard

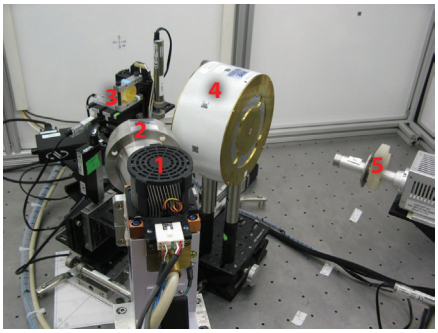

Figure 1. The hiRX breadboard instrument. Labels: **1**. X-ray source (Rh-anode, operated at 50 kV and 1 mA); **2**. Rh Kα (20.21 keV) excitation doubly-curved crystal (DCC); **3**. Sample holder, which is mounted on XYZ translation stages, providing the mapping capability of the instrument; **4**. Pu Lα (14.27 keV) collection DCC; **5**. Silicon drift detector (SDD). The instrument response was calibrated using six Pu-spiked surrogate spent fuel standards. Each standard or sample measured with hiRX consisted of a dried residue of a 1–2 µL deposit on Kapton film that was fixed within an XRF sample cell.

setup is described in Fig. 1). In hiRX, DCCs are used for both excitation and collection in order to reduce background signal and eliminate non-analyte peaks from the measured spectrum. The DCC's functionally is based on Bragg's law for X-ray diffraction. The crystals are toroidally bent and provide point-to-point focusing for one wavelength; multiple DCC segments are placed around the source-focus axis to increase signal intensity. Data for this study were collected in the form of Pu elemental maps, with total measurement times ranging from 45 to 165 minutes per standard or sample. The three samples for the study consisted of aliquots of bulk spent fuel with known total Pu content that were provided by Pacific Northwest National Laboratory and prepared as dried residues.

Pu elemental maps and corresponding optical images for both spent fuel sample A and a Pu-spiked standard B are shown in Fig. 2. The mass of Pu in each of the sample deposits was determined using the hiRX calibration and acceptable performance was demonstrated. The estimated limit of detection (LOD) for Pu in dried spent fuel residues was 375 pg. The detection and quantitation of Pu in spent fuel at concentrations < 200 ng/µL indicates that the hiRX sensitivity is more than adequate for detection of Pu in target spent fuel solutions, which nominally contain 1000 ng/µL.

Second-generation hiRX instrumentation to improve processing times

These results for the determination of Pu in spent fuel are very encouraging, but suffer from two limitations—namely, the need for sample preparation, i.e., drying and fixing, and the lengthy measurement time (45–165 minutes). In order to be deployed in an actual reprocessing environment, both sample preparation and analysis time must be reduced. This can be accomplished with the benchtop hiRX prototype (Fig. 3), which has a standard measurement time of 100 seconds. The benchtop prototype is compact (approximately 17×23×12 inches) and contains no moving parts. In contrast to the breadboard, which contains only a Pu Lα collection DCC, the prototype contains crystals for Pu Lα and U Lα, which allows simultaneous detection of both elements. This is important because spent fuel dissolver solutions typically have high U content which may exceed a 100:1 Pu/U ratio (g/L), impacting Pu peak deconvolution and quantitation. Sample preparation is faster as it only requires straightforward pipetting of liquid sample directly into an ultra-low volume microcell

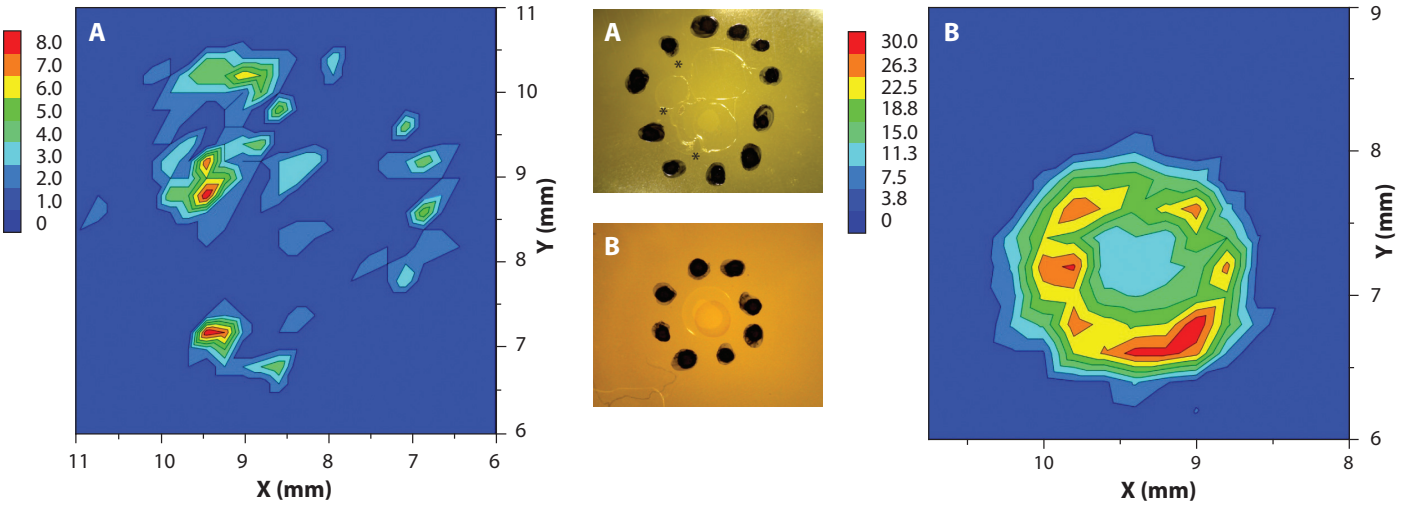

Figure 2. Elemental maps (left and right) and optical images (center) obtained using hiRX for spent fuel sample A (stars identify Pu hotspot regions seen in optical map A) and sample B, a 474 ng Pu spiked surrogate fuel standard.

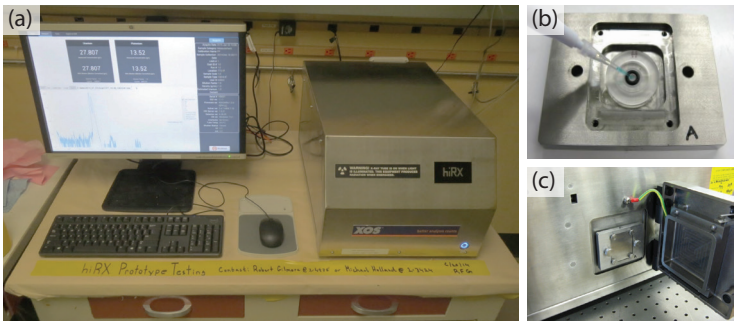

Figure 3. Images of: **(a)** The hiRX alpha-prototype instrument in field testing at Savannah River National Laboratory. **(b,c)** Sample preparation and measurement procedure.

and mounting in the instrument.

The prototype was recently field-tested at Savannah River National Laboratory (see Fig. 3) using process solutions from the Savannah River Site's H-Canyon. Results for Pu nitrate solutions were accurate (< 6% bias), and the speed and simplicity of the analysis was seen as an advantage over other methods. Other potential applications such as waste characterization were also identified.

Contaminated soil analysis

Sensitive detection of Pu in soil samples is important in nuclear forensics, safeguards, and environmental remediation. Elemental characterization can contribute to the understanding of the chemistry and fate of Pu in the environment, and in assessment of associated public health risks. This study of Pu in soil demonstrates the capability of lab-based, spatially-resolved characterization of heterogeneous matrices on the micrometer scale with nanogram sensitivity using complementary XRF techniques. Each approach has unique advantages depending on the type and level of characterization that is required, as described below.

We assessed the elemental composition of two soil particles contaminated with Pu using micro-XRF techniques, including hiRX and 3D confocal XRF. The bulk samples consisted of numerous soil particles from Los Alamos National Laboratory's TA-21 remediation site that were dispersed and fixed on a filter within an XRF sample cup. The bulk samples were first measured with the hiRX breadboard in order to identify soil particles of interest which contained Pu. While hiRX selectivity was indispensable to confirm Pu in two samples (referred to as C and D), its spatial resolution is limited by a 200 µm spot size, therefore we followed up using commercial micro-XRF instrumentation (Bruker M4 Tornado), which had higher resolution multi-elemental mapping capability based on a 25 µm spot size. Measurement times for 1.5×1.5 mm areas were approximately 20 minutes using this approach.

The distribution of Fe was chosen to represent the soil matrix, but other primary matrix components in the samples included Si, K, and Ca. Both samples were found to have discrete hotspots of Pu and Ti; sample C also had a Zn hotspot. Fig. 4 shows an optical image of the bulk soil sample and corresponding autoradiograph, in addition to an X-ray transmission radiograph of the soil particle of interest and micro-XRF elemental maps for sample D. While the autoradiograph indicates that radionuclides are present in the bulk sample, it is nonspecific for element and spatial location. The radiograph (10x) of sample D shows the Pu inclusion (Fig. 4c) as a high density particle of 30 µm diameter within the soil sample, which is approximately 800 µm across.

«« *An* **autoradiograph** *is an image produced by radiation from a radioactive object. A* **radiograph** *is an image produced by externally applied radiation.*

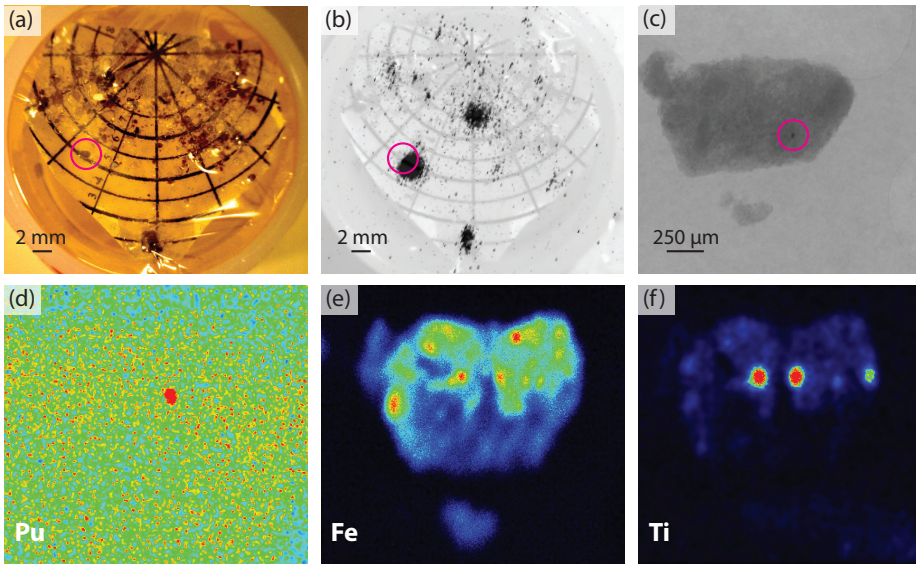

Figure 4. Top row: **(a)** Optical image of the bulk sample with soil particle D circled. **(b)** Autoradiograph of the bulk sample with soil particle D circled. **(c)** Radiograph (10x) of sample D with Pu inclusion circled. Bottom row: **(d–f)** Micro-XRF maps (1.5×1.5 mm) of Pu, Fe, and Ti distribution in sample D, respectively. The color scale indicates gross signal intensity, with cool colors (black, blue) for low count rates and warm colors (red, orange) indicating the highest count rates.

3D imaging gives greater insight into elemental distribution in soil particles

Confocal XRF was used to evaluate the elemental distribution within the soil particles in three dimensions, and showed a clear improvement over the two-dimensional measurements. The custom-built instrument includes an X-ray source and a Si-PIN diode detector, each equipped with a polycapillary optic, which allows characteristic X-rays to be discriminated in X, Y, and Z directions, and then visualized in 3D. During measurements, which lasted about 48 hours for sample D, XYZ stages slowly move the sample through the fixed confocal region, generating a series of data "slices". These 3D rendered images of samples C and D are shown in Figs. 6 and 5, respectively.

The confocal data for Pu and Ti for sample D agree closely with the micro-XRF results: there are three Ti hotspots (two intense and one less so) and a single Pu hotspot. Zn was also found throughout the soil sample with heterogeneous Cu distribution. Neither of these elements were readily detected by micro-XRF with dwell times up to 1 second per pixel, but were detected with the 3 second per voxel (3D pixel) dwell time using the confocal instrument. In order to further examine the element of interest (Pu) in sample D, a spectrum collected with the confocal instrument at the Pu hotspot revealed that Pu is co-located with Cu. The spectrum also contains a strong Fe peak and a moderate Zn peak, suggesting that the Pu is below the surface of the soil matrix. A spectrum collected at the nearby Ti hotspot,

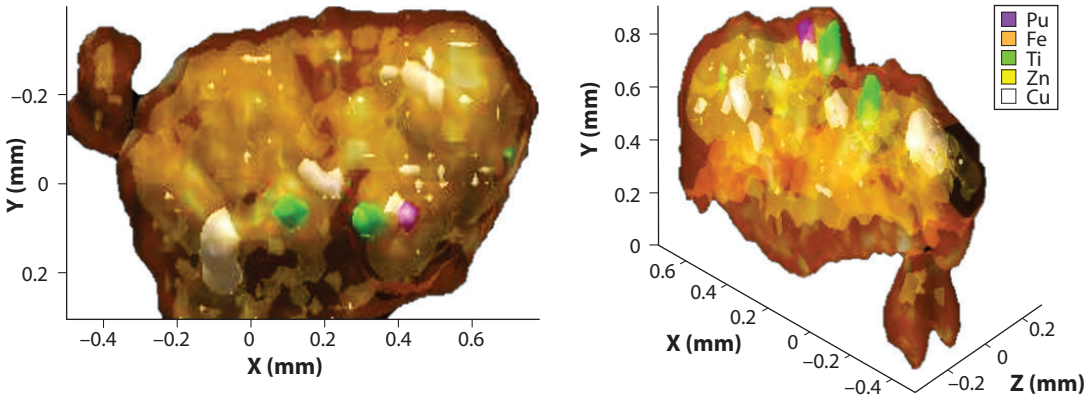

Figure 5. 3D rendered images showing elemental distribution in sample D, top down (left) and side view (right).

approximately 90 µm from the Pu concentration, showed peaks for Fe and Zn, but clearly indicates that neither Pu or Cu are present.

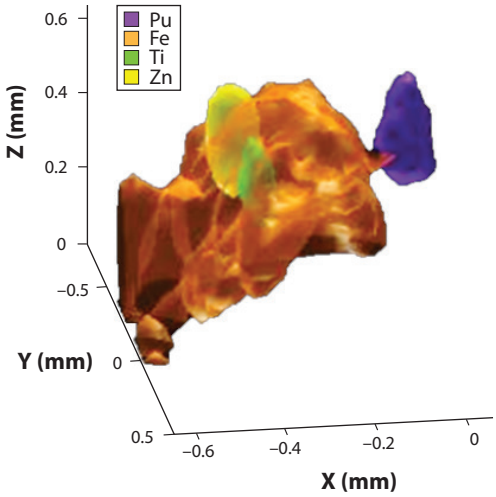

Figure 6. 3D rendered images showing elemental distribution in sample C, side view; total measurement time approximately 24 hours.

The 3D rendered image for soil sample C, which has not been covered in detail in this article, showed a considerably different result. This sample did not contain detectable levels of Cu and had a single Zn hotspot. Most notably, the Pu was located outside the Fe soil matrix. The Pu spectrum revealed that none of the soil matrix elements were detectable in that position, thus, the Pu is likely a PuO_2 particle (> 100 µm in diameter) that is associated with, but not incorporated within, the soil. This was not evident in 2D elemental maps. While speciation analysis would be required to assess the chemical form of Pu in each of the samples, the findings suggest that Pu may be present in multiple forms within soils collected from a single site, and that Cu and Fe may play a role in the complex chemical behavior of Pu within soils. The LOD for Pu in soil, as in sample D, is estimated to be < 15 ng for each of the three XRF methods.

Summary

This article focuses on our efforts to apply novel XRF instrumentation to two specific analytical challenges relevant to actinide science: quantification of Pu in a spent nuclear fuel matrix and characterization of Pu and co-located elements in a soil matrix. Both techniques are direct, lab-based, and nondestructive, leaving samples intact for archival or further study. These technologies are well suited for actinide and materials characterization as they allow for the study of a range of samples, from micron-sized agglomerates of nanomaterials to bulk materials, providing important information relevant to safeguards, the nuclear fuel cycle, material identification and attribution, and nuclear forensics. In particular, the hiRX and confocal XRF approaches provide highly specialized analyses that are difficult to obtain with other methods, yet have capabilities applicable to a myriad of sample types.

Further reading:

1. *K. G. McIntosh, S. D. Reilly, and G. J. Havrilla, "Determination of plutonium in spent nuclear fuel using high resolution X-ray," Spectrochim. Acta B 2015, 110, 1, 91–95.*
2. *K. G. McIntosh, N. L. Cordes, B. M. Patterson, and G. J. Havrilla, "Laboratory-based characterization of plutonium in soil particles using micro-XRF and 3D confocal XRF," J. Anal. At. Spectrom. 2015, 30, 7, 1511–1517.*
3. *K. G. McIntosh, G. J. Havrilla, R. F. Gilmore Jr, and M. K. Holland, "Evaluation of high resolution X-ray monochromatic wavelength dispersive X-ray fluorescence instrument for determining Pu and U in nuclear reprocessing streams," Spectrochim. Acta B 2018, in press; https://doi.org/10.1016/j.sab.2018.04.019.*

Acknowledgments

This work was supported by the LANL G.T. Seaborg Institute Postdoctoral Fellowship and the Office of International Nuclear Safeguards, National Nuclear Security Administration. The author gratefully acknowledges the following collaborators for their contributions: George Havrilla, Velma Lopez, Nikolaus Cordes, Brian Patterson, Sean Reilly, Evelyn Bond, Laura Wolfsberg, Hakim Boukhalfa, and Leah Arrigo.

Moving Actinide Science to New Extremes (of Pressure)

Matthew Jacobsen

Matthew Jacobsen was a Seaborg postdoc April 2015–March 2017, mentored by Nenad Velisavljevic. His work focused on designing high pressure apparatus for studying radioactive materials such as actinides. He is now a Research Staff Member at the Institute for Defense Analyses in Alexandria, VA.

»» *The* **Fermi level** *is the highest energy level occupied by electrons in a material at absolute zero temperature.*

The properties and structures of actinide materials are of great importance due to their wide ranging applications. For example, americium is a component of modern smoke detectors, uranium is a primary component of nuclear fuel materials and a possible contributor to internal heating of the Earth, and plutonium is a well-known component of nuclear weapons. In particular, there is great interest in investigating pressure (P) and temperature (T) as control parameters, as studies under high P and P-T regimes allow greater insight into the dynamics of f-shell systems and the unusual physics they bring. This is primarily through the controlled adjustment of atomic spacing in the crystalline structures. In particular, the light actinides (Th–Pu) exhibit a set of crystal structures not found elsewhere in the periodic table. Often distorted by narrow 5f bands close to the Fermi level, these crystal structures exhibit a range of interesting properties, including superconductivity and high strength, and the application of pressure is expected to force the heavier actinide elements into similar distorted structures.

Challenges under pressure

While interest in f-shell materials continues to grow, the range of applicable experimental techniques remains limited. Potential risks associated with radioactivity are often difficult to mitigate, and techniques can require direct sample access not available in many technologies, such as high pressure instrumentation.

In high pressure experiments, the timeframe of the measurements can also provide limitations. For example, in dynamic pressure studies (e.g., shock guns, the National Ignition Facility, and laser shock setups), measurement times are on the sub-microsecond scale and impractical for measuring properties like thermal conductivity, where second timescales are necessary. In addition, dynamic experiments couple temperature and pressure changes, making it difficult to isolate individual effects. Static pressure environments, meanwhile, do not have timescale restrictions, but have more limited physical access to the sample.

The most common static pressure system is a diamond anvil cell, composed of opposed diamond anvils sandwiching a sample within a metallic gasket. In these situations, non-contact techniques are required to resolve some properties. Other techniques for applying static high pressure exist, such as multi-anvil presses, which allow more flexibility to access the sample but are prohibitively difficult to contain. We have explored this class of static press to find a system that can allow both a range of useful physical measurements while providing a containment barrier from actinide radiation.

Containment vessel design

In an important step forward in the study of actinide materials under pressure, we have developed a containment vessel capable of probing elasticity and thermal parameters using simultaneous synchrotron X-ray and ultrasonic interferometry measurements. Typical safety requirements imposed at central user facilities, such as the Advanced Photon Source (APS), often require double or triple containment to ensure risk mitigation with regard to radioactive contamination. As described above, achieving such containment without jeopardizing the experimental setup is

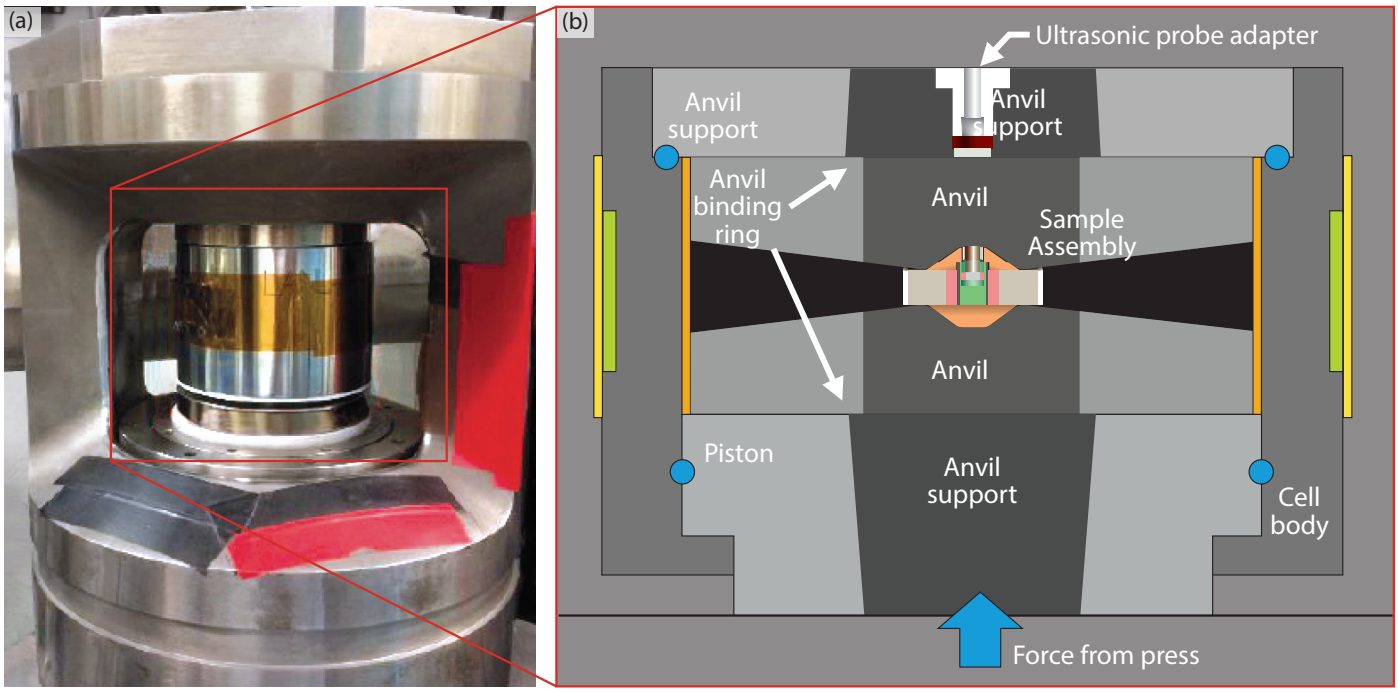

Figure 1. The openings of the Paris-Edinburgh press are optimal for the use of custom-designed setups, such as the containment vessel discussed here. **(a)** Despite the simple appearance, achieving containment in such a setup is challenging. Kapton tape (orange) and sapphire windows form the primary containment mechanisms used in this system. **(b)** The addition of the probe port through the top of the design allows for ultrasonic excitation of the sample.

difficult in both diamond anvil cells and multi-anvil presses. In contrast, the Paris-Edinburgh press (PE press), a large scale version of the diamond anvil cell, has proven flexible enough for both instrumentation and physical access to accommodate the containment vessel.

In such hydraulic presses, tungsten carbide is typically used in place of diamond, due to the expense and fragility of diamond. The upper anvil is fixed while the lower is actuated by hydraulic oil pressure. Large side openings and the freedom of motion between anvils and press frame allow insertion of specialized setups, such as a containment system. Our containment setup, shown in Fig. 1, is based on a previous design which allows for gas loading of samples and fits within the operational volume of the PE press (68×85 mm). Containment is achieved using a Kapton film barrier around the perimeter of the anvils and the external side of the can, with the sapphire optical/X-ray windows providing the third containment layer.

Ultrasonic interferometry

One distinct advantage of the PE press is the wide range of experimentation techniques that can be used with it. Therefore, development of a PE press containment vessel will be expected to broaden our current knowledge base by allowing the concurrent use of combined X-ray probes and other measurement techniques, with the potential to add more instrumentation techniques later. In particular, we have pursued one technique which shows promise—ultrasonic interferometry (UI). The UI technique involves generation of sound waves at a piezoelectric transducer, placed on the back of the upper anvil. The sound waves propagate through the anvil, buffer rod (Al_2O_3), and sample, and produce reflections at each interface (Fig. 2b). Transit times in the sample can be measured by overlapping reflections. For example, the reflection from the back surface of the sample (P2) is offset in time until overlapped with the top surface (P1) reflection. The sample thickness was measured radiographically (Fig. 2c), with sound velocities determined for both polarizations of wave propagation.

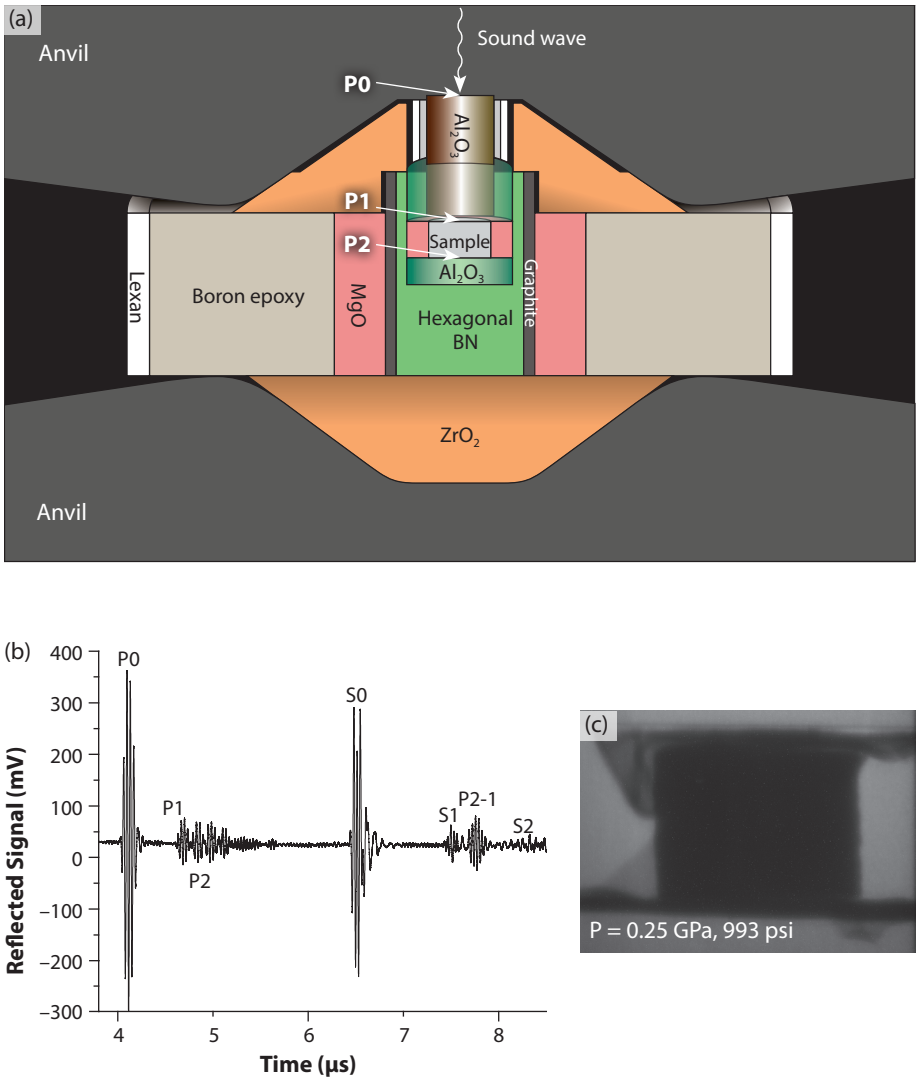

Figure 2. **(a)** Ultrasonic interferometry (UI) measurement of samples requires a composite gasket setup, with the sample and buffer rod located along the central axis of the setup. Location of reflections P0, P1 and P2 are indicated and correspond to signals below. **(b)** Externally generated sound waves then propagate through the anvil, buffer rod, and sample, with reflections generated at each interface; overlap of these reflections gives the round trip transit time for sound waves in the sample. **(c)** Sound velocities also include length determinations, performed from contrast imaging (radiography), at each pressure and temperature condition of interest.

Cerium dioxide and uranium studies

Cerium dioxide was the first sample chosen for these tests as it is not radioactive and, thus, safer to use for initial testing. Additionally, cerium dioxide has several magnetic and strength changes in its pressure-volume phase diagram that are interesting to investigate using these techniques. Initial tests on cerium dioxide and depleted uranium metal have shown promising results. Determination of the sound velocities has been achieved for CeO_2 and U up to pressures of 6 and 4.5 GPa, respectively, providing elasticity information at higher pressures than previously measured for either. Previous work has also shown that the sound velocities and X-ray properties allow a wide range of information to be extracted. For example, complete elasticity data for a material includes moduli (i.e., bulk, shear, Young's) and Poisson's ratio, which can be obtained through this technique. This data, in turn, informs us of how the material deforms, how it responds to temperature changes, and supports X-ray determination of strength. The sound velocities are also directly related to the elastic Debye temperature, acoustic thermal conductivity, and Grüneisen parameter, providing measures of the anharmonic behavior in addition to bonding characteristics.

Measuring thermal conductivity under extremes of pressure and temperature is very important for a variety of applications. For instance, it is theorized that the thermal conductivity of a material is dominated by contributions from electrons and acoustic phonons, with additional contributions from anharmonic effects and defects in the crystals. Thus, if the overall thermal conductivity or electrical conductivity is known, this data can be combined with the acoustic contribution determined from the sound velocities to estimate the contribution of the remaining factors. These insights facilitate studies into electron and phonon dynamics.

Detrimental effects on the experimental setup have also been explored; in particular, the angular range for diffraction and maximal pressure capacity. No restrictions to the accessible angles of diffraction were found to be created by the containment vessel (they are limited only by the PE press setup). Furthermore, the maximum achievable pressure in the PE press is 7–8 GPa for tungsten carbide anvils. The data gathered indicates that incorporation of the containment vessel into the PE press does not alter the available pressure range of the PE press, ensuring the full capability of the base press for experimentation.

Summary

We have developed and demonstrated the first and, currently, only experimental capacity for probing elasticity and thermal parameters of radioactive elements and compounds with pressure. Further improvements to this setup are underway and will soon include temperature as a parameter for such studies. This capability gives us a unique window into the internal lattice dynamics of f-electron systems and how pressure (and, soon, temperature) can be used to affect changes in the system. As a consequence, we will develop the ability to explore how crystalline structure, electronic topology, and many other phenomena affect the lattice as a whole. This first step towards taking actinide science to new extremes (of pressure and temperature) will help to significantly advance our understanding of these extraordinary elements and materials.

Further reading:

1. *M. I., McMahon, "High-pressure crystallography", Top. Curr. Chem., 2012, 315, 69–110.*
2. *A. Bocian, et al. "Gas loading apparatus for the Paris-Edinburgh press", Rev. Sci. Instrum., 2010, 81, 93904.*
3. *Y. Kono, et al. "X-ray imaging for studying behavior of liquids at high pressures and high temperatures using Paris-Edinburgh press", Rev. Sci. Instrum., 2015, 86, 072207.*
4. *M. K. Jacobsen, W. Liu, and B. Li, "Sound velocities of PbTe to 14 GPa: evidence for coupling between acoustic and optic phonons", J. Phys. Condens. Matter, 2013, 25, 365402.*
5. *M. K. Jacobsen, W. Liu, and B. Li, "Measurement setup for the simultaneous determination of diffusivity and Seebeck coefficient in a multi-anvil apparatus", Rev. Sci. Instrum., 2012, 83.*
6. *J. M. Ziman, Electrons and phonons: the theory of transport phenomena in solids, Oxford at the Clarendon Press, 1960, p20.*

Acknowledgments

The work presented in this article is from the collaboration between the author and Nenad Velisavljevic at Los Alamos National Laboratory. This work was performed using the facilities of beamline 16-BM-B of the Advanced Photon Source. The author gratefully acknowledges the support of the U.S. Department of Energy through the Los Alamos LDRD program and the G.T. Seaborg Institute.

Keri Campbell

Keri Campbell was a Seaborg fellow 2015–2017, mentored by Elizabeth Judge and James Barefield. Her field of study was radiochemistry, focusing on nuclear safeguards and nuclear forensics. She is now a staff scientist in the Chemical Diagnostics and Engineering group (C-CDE).

A Promising Tool for Nuclear Safeguards: Laser-Induced Breakdown Spectroscopy

The ability to directly examine elemental and isotopic concentrations in nuclear fuels without dissolution of material is of interest to nuclear safeguards, nuclear forensics, and nuclear fuel performance evaluations. Each of these missions have different needs for characterization of nuclear material, including qualitative and quantitative analysis of major and trace elements, isotopic analysis, phase identification, and physical analysis. The common ground between these missions is the need for a fast and reliable non-destructive assay technique. Laser-induced breakdown spectroscopy (LIBS) is a rapid technique for direct solid sampling in analytical chemistry which we have explored for this purpose. LIBS is very useful because it analyzes samples directly (reducing the risk of contamination), it does not require destructive dissolution of the samples, it can determine the spatial distributions of the various elemental compositions, and it is readily deployable.

The international nuclear forensics community has reached a consensus in the sequencing of techniques to provide valuable information as early as possible during the attribution process. The timeline identifies techniques to be performed within 24 hours, one week, or one month. LIBS has the potential to meet the challenges of phase identification and measure major and minor elements in interdicted samples within a timeline of hours after receiving the sample. Other studies have demonstrated the ability of LIBS to measure major and minor constituents in uranium samples, perform isotopic analysis, and quantitatively determine the concentration of uranium in various matrices. These studies have shown the ability of LIBS to determine attributes of interest to the nuclear forensic community.

Instrumentation

LIBS is a type of atomic emission spectroscopy that uses a laser as the excitation source to form micro-plasma on the sample surface. The sample is ablated in nanogram quantities and incorporated into the micro-plasma. As the plasma expands and cools, the excited atoms emit characteristic light specific to each element. The emitted light is then optically collected, guided to a spectrometer for detection, and time-resolved with a digital delay generator. Optimization of the timing allows us to discriminate the signals of interest from the background continuum. The resolving power of the spectrometer and signal-to-noise ratios are important for instrument and experimental parameters when actinides are in the matrix of interest. Resolving power helps to isolate an atomic emission line from neighboring transitions that may be of the same element that have a different concentration dependency, or of an entirely different element. The simplicity of the LIBS experimental instrumentation enables broad versatility in application space. For instance, it can be coupled to a glovebox or used in a hot cell for analysis in high-ionizing radiation areas. Each component in Fig. 1 can be downsized into a person-portable system, such as a backpack or a handheld device.

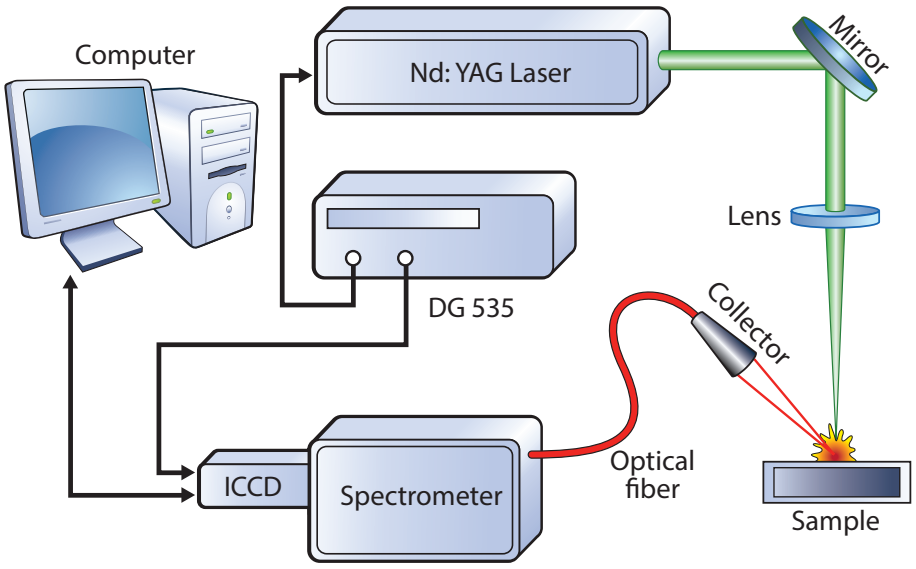

Figure 1. Schematic of the laser-induced breakdown spectroscopy (LIBS) setup. The combination of the ICCD (intensified charge-coupled device) camera and spectrometer is key for time-resolved spectroscopy. The "DG 535" unit is a digital delay and pulse generator.

Our research group at Los Alamos National Laboratory (LANL) has contributed extensively to the advancement of LIBS as an analytical tool for nuclear forensics and nuclear safeguards. We have analyzed samples related to the nuclear fuel cycle, from uranium ores to simulated used nuclear fuels. Matrix effects of uranium, in addition to system components (resolving power of the spectrometer), have been evaluated for determining limiting factors, such as detection limits, for elements and isotopes of interest to nuclear safeguards and nuclear forensics. Depending on the experimental setup and the matrix, the limit of detection (LOD) for uranium is on the order of 100 to 50,000 ppm. The larger LOD values were measured with uranium ore samples, a low-resolving power spectrometer, and a sample-instrument distance of ~2 meters.

Determination of burn-up rates using metal analysis

Analysis of burn-up rates for fuel samples obtained from countries of interest can indicate whether a reactor is producing weapons-grade plutonium. If the reactor is being used for peaceful purposes such as energy production, the plutonium isotopes are not ideal for weapon production. Quantification of the metals found in the epsilon phase (Rh, Ru, Pd, and Mo) are the best indicators for burn-up rates, since their concentrations increase linearly with burn-up. Our team has successfully determined LODs for these metals using LIBS, along with zirconium and cerium in simulated used nuclear fuels. The simulated used nuclear fuels in the analysis were based on the light water reactor fuels most commonly used globally (UO_2 matrix). It was found that the concentrations of elements of interest to nuclear safeguards can be determined by LIBS, with LODs relevant to low burn-up rates.

Actinide determination

Studies have also been performed to qualitatively identify plutonium, americium, and neptunium in a uranium oxide matrix, coupling the LIBS system to a glovebox at LANL's PF-4 facility. Although the experimental setup is simple, the spectrum is complex when actinides are present in the matrix. Over 980 unique emission lines were assigned in the mixed actinide sample spectra, and a myriad of emission lines were found to have interferences from other elements. Care must be taken when choosing an emission line of interest to ensure it is concentration dependent and does not have spectral interferences with other elements in the matrices. This work highlighted the utility of LIBS not only in safeguards, but also as quality control for a mixed oxide (MOX) fuel fabrication facility.

«« **MOX fuel** *is a type of nuclear fuel that contains mixtures of different oxides, e.g. a mix of plutonium and uranium, (U,Pu)O_2. It is a way of utilizing surplus weapons-grade plutonium, which otherwise would have to be stored under high security.*

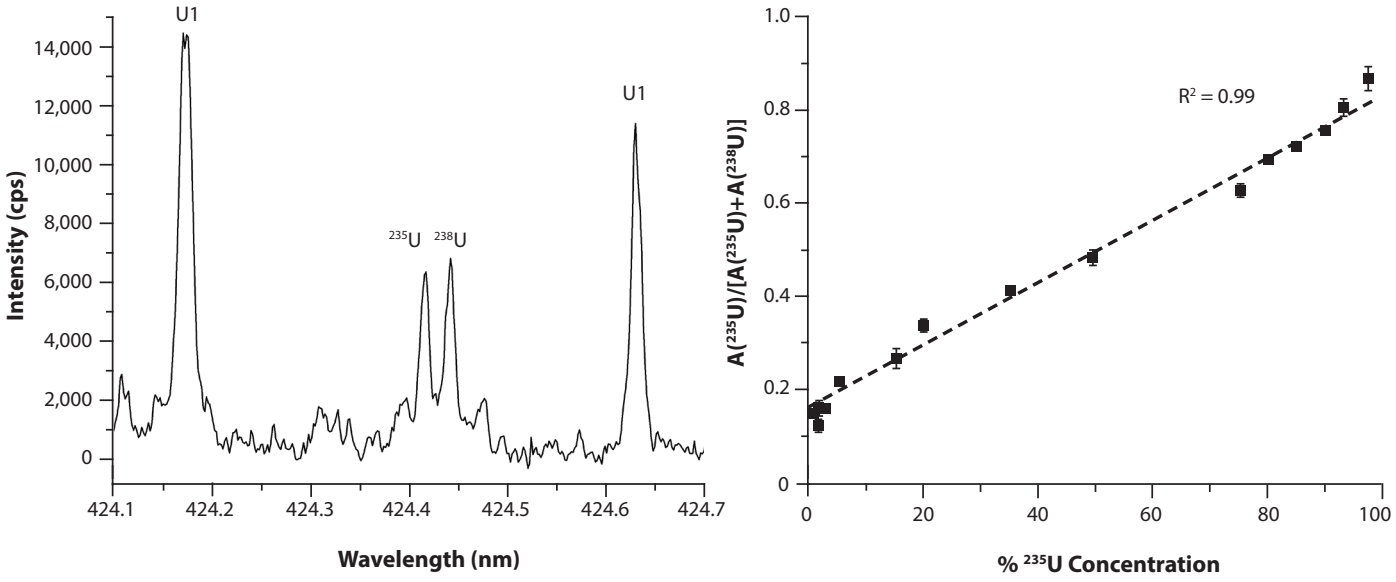

Figure 2. Representative LIBS isotopic analysis of uranium: **(a)** LIBS spectrum of 49.6% ^{235}U in a powder matrix, highlighting the 424.437 nm isotope shift; **(b)** Quantification of uranium via direct spectral analysis of peak area by taking the ratio of $^{235}U/ (^{235}U + ^{238}U)$ and plotting the ratioed area to the known ^{235}U wt.% composition. The calibration curve has a correlation coefficient (R^2) of 0.99 and provides a data analysis method that can be used to quantify isotopic compositions of unknown samples.

Phase identification

In nuclear forensics, it is important to obtain phase identification (the chemical/physical form which the elements are in) for the samples of interest. LIBS is a rapid technique that has the potential to meet the challenges of phase identification in interdicted samples within a timeframe of less than an hour after receiving the sample, including data analysis. Using an argon gas environment, one can compare the ratios of atomic emission lines from uranium and oxygen as a way to discriminate between different uranium oxide phases commonly found throughout the nuclear fuel cycle. We were successful in discriminating between UO_3, UO_2, and U_3O_8—this technique does not deduce crystalline structure, rather the ratio of the elements of interest. A selection of uranium and oxygen emission lines were also successfully modeled using the Los Alamos suite of atomic physics codes, which helps to understand the role of f-orbitals in plasma dynamics.

Isotopic ratios

Not only can LIBS quantify elements of interest in complex matrices, it can also quantify major isotopic ratios. Isotopic analysis reported in the literature relies on the isotope shift of the 424.437 nm emission line of uranium. An example of isotopic measurements of $^{235}U/^{238}U$ is shown in Fig. 2a. The resolving power of the spectrometer needs to be at least 17,000 to resolve the $^{235}U/^{238}U$ isotope shift, and greater than 100,000 to resolve the $^{234}U/^{235}U$ shift. Furthermore, the concentration of minor uranium isotopes needs to be significant in order to background-resolve the peaks (similar to the LOD for elemental uranium). For these reasons, measurements of the minor isotopes using LIBS are not reported in literature. Using a spectrometer with an appropriate resolving power, LIBS can distinguish between depleted, low-enriched, and high-enriched uranium. A suite of uranium oxide powders with enrichments ranging from 1–97% ^{235}U were analyzed using a high-resolution spectrometer. The results from the data analysis, shown in Fig. 2b, indicate that LIBS can determine the enrichment of uranium powders across the range of interest for nuclear safeguards and nuclear forensics. Less than 1 μg of the sample is consumed during the sampling process.

Summary

LIBS is a robust technique that can fill gaps identified using current technologies—it is rapid (depending on the application, analysis within minutes), is field-deployable, uses direct sample analysis, and can detect all known elements. This technique could be used as a standalone analysis of samples of interest to the nuclear community, or implemented as a screening technique to identify potential samples of interest for further characterization. We have demonstrated the ability of LIBS to determine attributes of interest for nuclear forensics, nuclear safeguards, and nuclear fuel performance evaluations. Using LIBS would minimize the number of steps in the handling process and maximize throughput and turnaround time compared with current non-destructive assay techniques, with the ability to determine major isotopic ratios and concentrations of elements of interest, in a multitude of matrices.

Further reading:

1. *E. J. Judge, J. E. Barefield II, J. M. Berg, S. M. Clegg, G. J. Havrilla, V. M. Montoya, L. A. Le, and L. N. Lopez, "Laser-induced breakdown spectroscopy measurements of uranium and thorium powders and uranium ore", Spectrochim. Acta B, 2013, 83–84, 28–36.*
2. *J. E. Barefield II, E. J. Judge, J. M. Berg, S. P. Wilson, L. A. Le, and L.N. Lopez, "Analysis and spectral assignments of mixed actinide oxide samples using laser-induced breakdown spectroscopy (LIBS)", Applied Spectroscopy, 2013, 67:4, 433–440.*
3. *J. E. Barefield II, E. J. Judge, K. R. Campbell, J. P. Colgan, D. P. Kilcrease, H. M. Johns, R. C. Wiens, R. E. McInroy, R. K. Martinez, and S. M. Clegg, "Analysis of geological materials containing uranium using laser-induced breakdown spectroscopy", Spectrochim. Acta B, 2016, 120, 1–8.*
4. *K. R. Campbell, E. J. Judge, J. E. Barefield II, J. P. Colgan, D. P. Kilcrease, K. R. Czerwinski, and S. M. Clegg, "Laser-induced breakdown spectroscopy of light water reactor simulated used nuclear fuel: Main oxide phase", Spectrochim. Acta B, 2017, 133, 26–33.*
5. *K. R. Campbell, N. R. Wozniak, J. P. Colgan, E. J. Judge, J. E. Barefield II, D. P. Kilcrease, M. P. Wilkerson, K. R. Czerwinski, and S. M. Clegg, "Phase discrimination of uranium oxides using laser-induced breakdown spectroscopy", Spectrochim. Acta B, 2017, 134, 91–97.*

Acknowledgments

The author gratefully acknowledges the support of the U.S. Department of Energy through the G. T. Seaborg Institute, the LANL Laboratory Directed Research and Development (LDRD) Program, and Defense Threat Reduction Agency (DTRA) for this work.

Jason K. Ellis

Jason Ellis was a Seaborg Fellow from July 2013 to January 2015. He studied the properties of thorium materials predicted by screened hybrid density, and was mentored by Richard Martin. He is currently Vice President of Engineering at Dimensional Mechanics, Inc.

»» *A* **nuclear excitation** *is a transition between two different states of the nucleus of an atom, similar in many ways to electronic transitions that underpin various common technologies.*

»» *A* **nuclear clock** *is a hypothetical improvement to the atomic clock which would be expected to be more accurate. In the atomic clock, the unit of time is based on the frequency of electronic transitions within an atom's shell, whereas a nuclear clock would use the frequency of nuclear transitions within the atom's nucleus.*

Towards a Nuclear Clock: Theoretical Studies of Thorium Materials for the Direct Measurement of the Lowest-Lying Nuclear Transition in ^{229}Th

Fundamental research into the properties of actinide isotopes continues to be of paramount importance for developing new materials and technologies vital to our national interests. This research continues to find applications in the science of signatures, improving the accuracy of GPS technology, and maintaining and modernizing our nuclear stockpile and infrastructure.

For several years there have been ongoing attempts to directly measure the lowest-lying nuclear excitation of thorium-229. In the 1970s, nuclear spectroscopy identified this state and recent indirect measurements indicate that the transition energy should be 7.8 ± 0.5 eV, an energy that corresponds to a wavelength of 160 ± 10 nm. This wavelength is within the region of the spectrum known as the vacuum ultra-violet (VUV), a range now accessible to state-of-the art lasers; this discovery has therefore stimulated significant interest for directly measuring this nuclear transition in ^{229}Th using optical spectroscopy. Direct measurements probe the existence of a single transition whereas indirect measurements capture all the light emitted from a source and therefore cannot determine which state transitions are responsible for the light observed. A successful direct measurement would open a variety of avenues in both fundamental and applied research; in particular, it may lead to the development of a solid-state "nuclear" clock with an accuracy more than an order of magnitude more precise than the current state-of-the-art atomic clock, as well as the direct manipulation of the quantum state of an atomic nucleus using solid-state lasers.

Unfortunately, ^{229}Th has no natural abundance on Earth; it is a product of α-decay of ^{233}U, a highly-controlled Special Nuclear Material. Therefore, high quality theoretical predictions of the properties of these materials are extremely valuable to guide experimental efforts. Fortunately, ^{232}Th has the same electronic structure as ^{229}Th, so theoretical predictions may be experimentally tested using this more abundant isotope, though such experiments still require stringent safety and security precautions.

Experimental approach

One of the leading proposals for measuring this transition developed at Los Alamos National Laboratory (LANL) involves embedding ^{229}Th into a solid-state crystal, and directly probing the nucleus using a VUV laser. The crystal needs several properties to be a good candidate material. First, the material needs to be transparent to (i.e., have a band gap greater than) the VUV spectrum, otherwise the nucleus cannot be excited by the laser, and any luminescence would be absorbed by

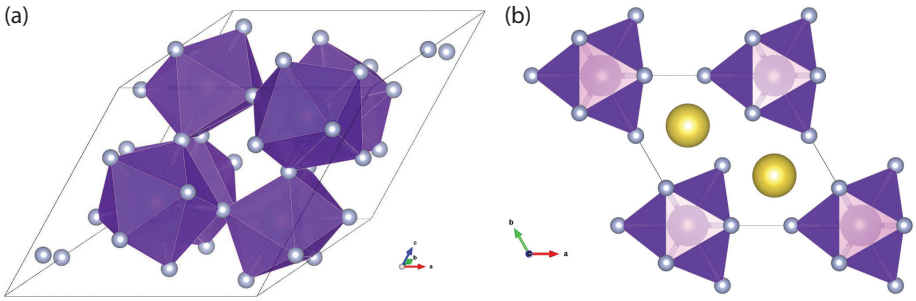

Figure 1. Unit cells for the crystal structures of **(a)** ThF_4 and **(b)** Na_2ThF_6, with thorium indicated in purple, fluorine in grey, and sodium in yellow. Polyhedra indicate fluorine coordination around thorium atoms.

the electrons. Second, the material should accommodate the Th^{4+} oxidation state to minimize inhomogeneous broadening of the fluorescence signal. Finally, the material should be one in which the ^{229}Th-doped crystal can be grown with high purity and few defects, so that color center defects do not interfere with the excitation of and emission from the ^{229}Th nuclei. Within these constraints, several possible materials have been proposed, including Na_2ThF_6, ThF_4, MgF_2, $LiCaAlF_6$, and CaF_2. These are all wide band gap (> 10 eV) materials that should possess the necessary properties.

Modeling approach

To understand the electronic structure and properties of these candidate materials, we employed both density functional theory (DFT) and a more accurate and computationally expensive many-body Green's function approach (G_0W_0). Since the 1960s, electronic structure calculations using DFT have successfully predicted a wide variety of material properties. Although in principle DFT is an exact theory, in practice, the exact exchange-correlation functional is not known. Successive generations of density functionals —local density approximation (LDA), generalized gradient approximation (GGA), and hybrid functionals—have enjoyed success for a wide range of problems. However, these functionals often fail for strongly correlated materials (i.e., materials which cannot be described as non-interacting entities), such as actinides.

The screened hybrid functional of Heyd, Scuseria, and Ernzerhof (HSE) successfully predicts the properties of a variety of actinide oxide insulators. Screening the Coulomb potential at long range significantly improves the computational efficiency. To accomplish this, screened hybrid functionals, such as HSE, separate the inter-electronic Coulomb potential into short- and long-range components. After fitting this functional to a broad class of known materials, the short-range screening parameter can be determined, eliminating all the material-dependent parameters. Therefore this functional can make theoretical predictions about the properties of materials outside the fitting set. HSE successfully predicts the experimentally observed band gaps of conventional semiconductors, and even the problematic Mott insulators. It is important to note that typical gaps in these materials are of the order of a few eV, while conventional DFT incorrectly predicts them all to be metallic, i.e., possessing no band gap at all.

Although the HSE functional proved quite successful for small- to medium-gap semiconductors and insulators (gaps < 6 eV), recent work indicates that it systematically underestimates the band gaps of wide gap (> 6 eV) materials by up to 1–2 eV. This work showed that a many-body approach, now known as the GW method and first introduced by Lars Hedin in Physical Review in 1965, improves upon this, although it too yields gaps typically an eV lower than experimental data for large (> 8 eV) gap materials.

The many-body Green's function (G_0W_0) approach

This alternative approach to using DFT involves calculating the one-particle

«« In general, a **functional** *is a mathematical term given for a function of a function. In DFT, functionals are functions of spatially-dependent electron density in an atom. These sets of equations represent the core component of the theory.*

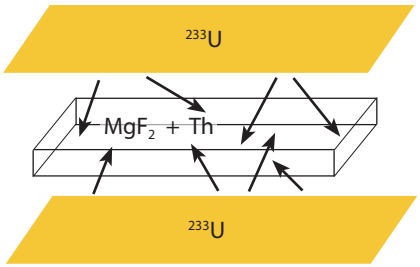

Figure 2. A plate of MgF_2 is exposed to ultra-pure (99.999%) ^{233}U, which decays to release ^{229}Th and alpha particles that embed in the MgF_2 plate.

»» *A* **Green's function** *is a device used to solve difficult ordinary and partial differential equations which may be unsolvable by other methods. In this context, the one-particle Green's function refers to the solution of the approximated many-body Schrödinger equations obtained using the Green's function approach.*

Green's function of an interacting electron. In this method, the correlation effects of the many-body system are incorporated in the calculation of the one-particle self-energy operator. In contrast to DFT, where uncertainty in the calculation arises from not knowing the exact form of the exchange-correlation functional, in the GW approach the uncertainty comes from various levels of approximation in calculating the self-energy operator. The simplest (0th order) version of the GW approach, known as G_0W_0, has been implemented in the VASP software package, among others.

ThF_4 and Na_2ThF_6

The known crystal structures of the two candidate materials, ThF_4 and Na_2ThF_6, are presented in Fig. 1. In both of these materials, ^{229}Th can be easily incorporated into the crystal by direct substitution for ^{232}Th during crystal growth. This allows precise control of the ^{229}Th concentration in the crystal. The fluorine atoms surround the thorium in a trigonal tri-capped arrangement in Na_2ThF_6 (Fig. 1a), whereas the thorium sits at the center of a distorted octahedron in ThF_4 (Fig. 1b). We found, as expected, that HSE predicts smaller gaps for these materials than G_0W_0 does—HSE predicts 8.9 eV for both materials, whereas G_0W_0 predicts gaps of 10.1 and 11.1 eV for ThF_4 and Na_2ThF_6, respectively. Our HSE calculations give an effective lower boundary for the theoretically predicted band gap of these materials. As the HSE predicted gap lies approximately 1 eV above the predicted nuclear transition energy, we conclude that either of these materials would be suitable candidate materials. That said, our best estimate (from the G_0W_0 calculations) indicates that Na_2ThF_6 would be a better choice, because it has a larger gap.

Th-doped MgF_2

In addition to these stoichiometric candidate materials, there is an ongoing experimental effort at LANL to measure this transition in ^{229}Th-doped MgF_2. In these experiments, a plate of MgF_2 is exposed to an ultra-pure sample of ^{233}U for a fixed length of time (Fig. 2). As ^{233}U decays, it emits ^{229}Th nuclei and alpha particles that impact and embed in the MgF_2 plate. The total concentration of ^{229}Th embedded in the plate is determined by the exposure time, and a higher concentration of ^{229}Th increases the magnitude of the experimentally observable signal. This type of isotope implantation experiment presents a number of challenges not present when using lab-grown crystals that we have addressed using similar electronic structure calculations.

The first question to answer is what is the most energetically favorable oxidation state of ^{229}Th in doped MgF_2? We performed a series of calculations in which we considered a variety of charge-compensating defects to compare the +2, +3, and +4 oxidation states of the thorium atom. Since magnesium is found in the +2 oxidation state in MgF_2, directly substituting Th in a Mg^{2+} site formally puts thorium in the same oxidation state. To obtain the +3 oxidation state, we examined the addition of a single fluorine atom near the Th site. To achieve a +4 oxidation state, there are two symmetry-allowed charge compensation schemes to consider. First, removing a near-neighbor magnesium atom, and second, adding two nearby fluorine atoms.

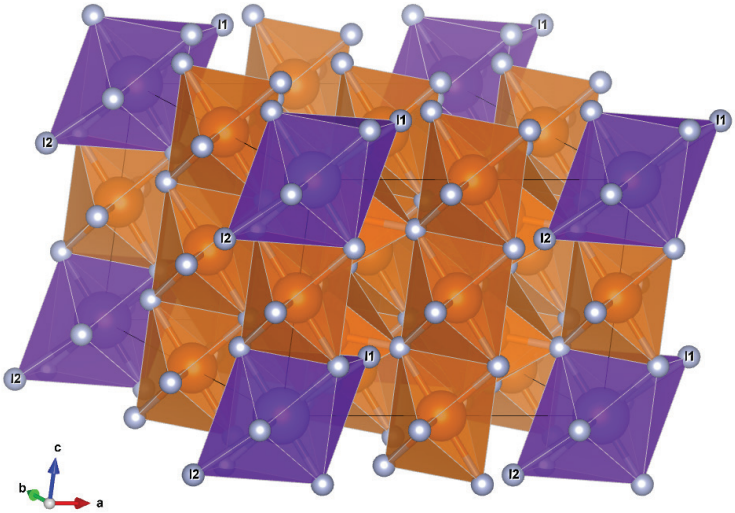

Figure 3. Using a 2×2×2 supercell of MgF_2 doped with thorium (purple), we find the lowest energy local configuration requires two fluorine interstitial atoms to compensate the thorium in the +4 oxidation state.

To understand this, our calculations were carried out on a 2×2×2 supercell, and we performed a complete geometry optimization, relaxing both the atomic positions and the lattice vectors. Comparing the absolute energies, we found that the most energetically favorable scheme was the +4 oxidation state charge compensated with two fluorine interstitial atoms (Fig. 3).

Band gap calculations in doped MgF_2

We sought to understand how the presence of ^{229}Th affects the band gap of doped MgF_2. If the addition of a thorium atom and interstitial fluorine atoms decreases the band gap so it becomes smaller than the energy involved in the nuclear transition, then competing processes other than direct photon emission become possible and could make the photon emission channel very weak (leading to a very weak, if not unobservable signal).

Our HSE calculations on the undoped crystal predict a gap of 9.0 eV, which underestimates the experimental gap of 12.2 eV, whereas our G_0W_0 calculation is much closer with a gap of 11.5 eV. As before, we expect the HSE calculations to provide a lower bound for the band gap in the doped crystal. These calculations predict the thorium f-band to lie directly below the Mg s-bands in the undoped crystal, shrinking the calculated band gap to 8.3 eV. This lies 0.5 eV above the indirect measurement of 7.8 eV for the nuclear transition, at the extreme of the experimental uncertainty. Our G_0W_0 calculation meanwhile predicts a gap of 10.2 eV, more than 2 eV greater than the nuclear transition. We therefore conclude that it should be possible to directly observe the photon emission associated with the nuclear transition in ^{229}Th-doped MgF_2.

Summary

These results inform ongoing experimental efforts at LANL to directly measure the nuclear transition in ^{229}Th. Once this transition has been measured, we will be uniquely positioned to begin experiments that directly manipulate the nucleus of an atom using optical spectroscopy; for example, by driving this transition using a laser, one can construct a so-called "nuclear clock". In addition, by directly manipulating the state of the atomic nucleus, it becomes possible to study how the nucleus absorbs and emits a photon, giving us greater insight into the fundamental forces that bind the protons and neutrons together. This major scientific breakthrough would open the door to a wide variety of fundamental research as well as exciting new applications.

Acknowledgments

This work was supported under the Heavy Element Chemistry Program at LANL by the Division of Chemical Sciences, Geosciences, and Biosciences, Office of Basic Energy Sciences, U.S. Department of Energy. Portions of the work were also supported by the LDRD program at LANL. Jason Ellis gratefully acknowledges a Seaborg Institute Fellowship. LANL is operated by Los Alamos National Security, LLC, for the National Nuclear Security Administration of the U.S. Department of Energy under contract DE-AC5206NA25396.

Magnetic Resonance for Actinide Science: A Perspective

Michael Malone

After four years as a research analyst at Fannie Mae, Michael Malone began a PhD in Physics at George Mason University in 2008. Graduating in 2013, Dr. Malone began a postdoctoral appointment at Los Alamos National Laboratory (LANL) where his research included observing water uptake in trees via low-field NMR (mentored by Sanna Sevanto) and extending his graduate research in explosives detection via NQR (mentored by Michelle Espy). With guidance from Marianne Wilkerson he received a Seaborg Fellowship to pursue magnetic resonance studies of actinide compounds. He is currently a staff scientist at LANL (P-21) continuing to study novel applications of NQR and other sources of weak magnetic fields relevant to national security concerns.

Magnetic Resonance (MR) is a field that spans many disciplines, including physics, chemistry, and biology, and consists of various techniques, e.g., Magnetic Resonance Imaging (MRI), Nuclear Magnetic Resonance (NMR), Electron Paramagnetic Resonance (EPR), and Nuclear Quadrupole Resonance (NQR). The unifying principle between these techniques is the observation of oscillating magnetic fields from atomic nuclei to extract information about a sample (with the exception of EPR, which interrogates electrons). The information obtained from an MRI scanner in a hospital is well known—it is a visualization of the inside of the body. For the other techniques, the extracted information can be less apparent: NMR can, for example, reveal the identity of small molecules, the structure of proteins, or the fat content of a salmon fillet; NQR can detect hidden narcotics such as cocaine in mail, or the temperature distribution of material; EPR can determine the chemical nature of a free radical or the biochemical activity of an enzyme (Fig. 2).

Only certain nuclei are amenable to MR techniques. Principally, they need to be magnetic, and in the language of physics we say they need to have a nuclear spin greater than 0. The most common target of MR techniques is the hydrogen nucleus, i.e., the spin-½ proton. Protons are targeted due to their prevalence (especially in organic molecules), their symmetrical charge distribution (associated with all spin-½ nuclei), and their large gyromagnetic ratio, a factor which tells us about the strength of the oscillating magnetic field they can produce and the ease with which they can be observed. While most nuclei have stable isotopes that can, in principle, be detected with MR, in practice this is not always practical. For instance, helium is the second-most abundant element in the universe, but almost all of it exists as spin-0 helium-4, which cannot be directly observed with MR. Additionally, many nuclei have charge distributions that are not spherical (i.e., they have spin greater than ½). Instead they can be prolate, like a football, or oblate, like a pumpkin (Fig. 1). The deviation from a spherical form is measured by the quadrupole moment, and its presence can complicate the interactions of the target nuclei, making their observation in NMR, at least, much harder.

Actinide MR

Actinide nuclei in particular are very challenging to observe in MR, with the first challenge being administrative. Access to large quantities of these materials can

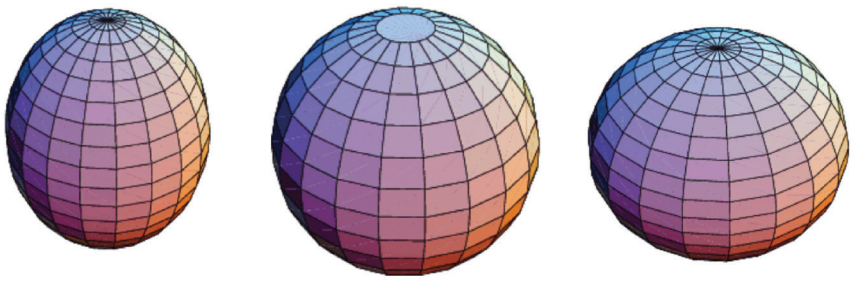

Prolate Spheroid | Sphere | Oblate Spheroid

Figure 1. In atomic nuclei, the charge distributions of their unpaired nuclear spins are not always symmetrical. The symmetrical case is spherical, center, for a spin-½ nucleus such as hydrogen. Nuclear spins greater than ½ can create asymmetric distributions as shown on the left and right with prolate and oblate spheroid forms. This can create more complex spectra which are more difficult to interpret. Image source: Wolfram Mathworld (*mathworld.wolfram.com*).

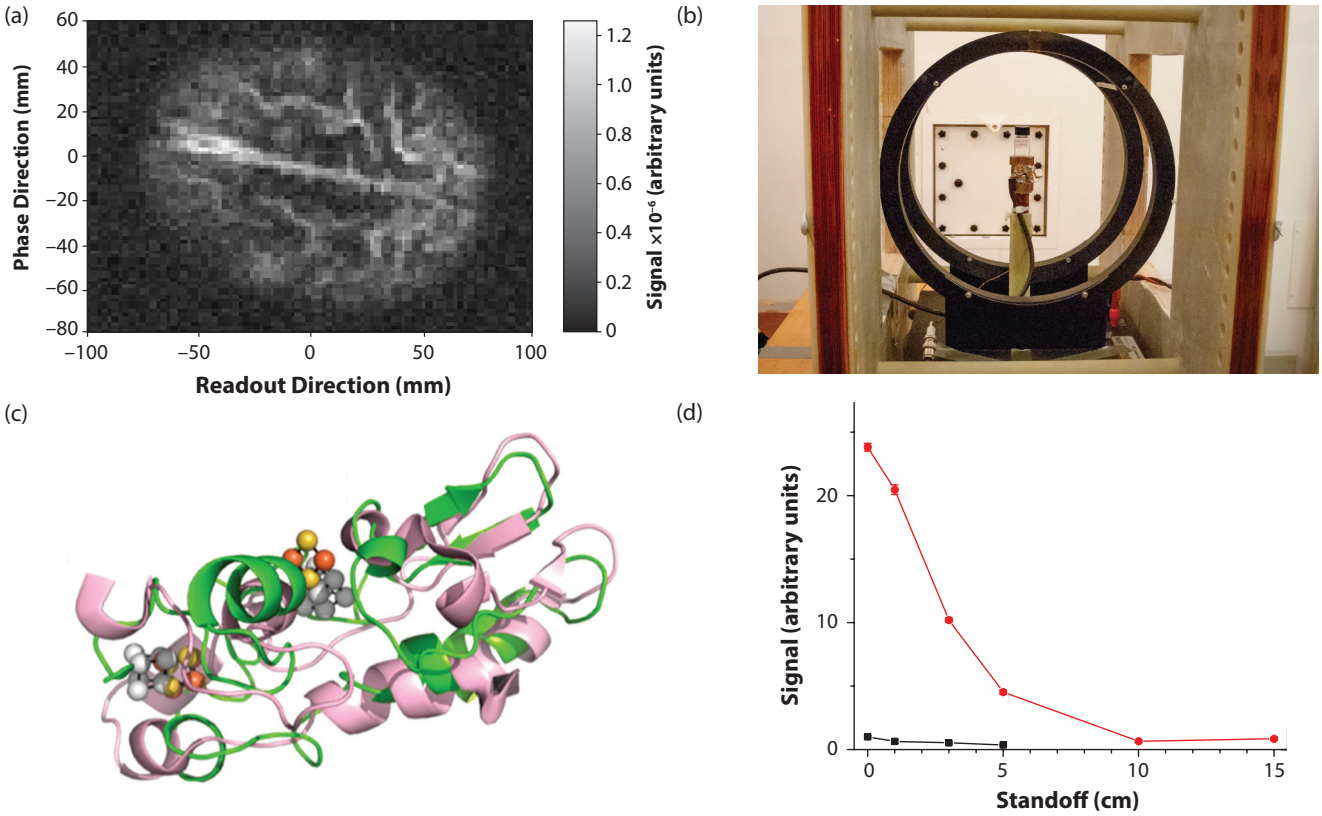

be heavily restricted, greatly reducing the number of laboratories that can attempt experiments, and the number of experimentalists that can develop techniques. The second major challenge is that actinides tend to have weak signals due to their low gyromagnetic ratios: plutonium-239 and uranium-235 have gyromagnetic ratios 7% and < 2% of hydrogen's, respectively (see Table 1). And while the spin-½ plutonium-239 nucleus has a spherical charge distribution, uranium-235 has an extremely large quadrupole moment, greatly increasing the difficulty of its observation with NMR-based techniques. Additionally, plutonium and uranium molecules tend to be paramagnetic (i.e., they possess unpaired electrons), a property that makes their observation in NMR more challenging, although such compounds can be analyzed using EPR, which targets the paramagnetic properties of a material.

Capabilities to observe actinide nuclei directly with MR have many applications. Most importantly, they can detect compounds of interest to Los Alamos National Laboratory's (LANL's) global security missions, without the need for expensive helium-3 detectors or deuterium-tritium electronic neutron generators. MR signals can determine actinide enrichment as their intensity is proportional to the relative density of the target nuclei. In comparison to enrichment measurements made via mass spectrometry, MR techniques can be performed on the bulk sample, remotely, non-destructively, and with the potential for a field-capable, handheld device. Additionally, MR techniques could provide a direct measurement of nuclear interactions in their local (molecular) environment, for instance, to determine the chemical nature of bonds, such as bond distances and angles, in ways not accessible through other techniques. This could be used in the analysis of nuclear waste and fuels, separations chemistry and fundamental actinide science. Finally, NQR in particular has been used to measure the aging of materials and compare production techniques, suggesting a technique with multiple applications.

Figure 2. Magnetic resonance techniques have a broad range of applications: **(a)** A low-field Magnetic Resonance Imaging (MRI) image of a brain taken at LANL reveals a stroke to a trained radiographer. **(b)** This low-field Nuclear Magnetic Resonance (NMR) system developed at LANL utilizes dynamic nuclear polarization to dramatically enhance the signal from nuclei with small gyromagnetic ratios. **(c)** Electron Paramagnetic Resonance (EPR) can be used to interrogate the active sites of large metalloenzyme molecules, such as the radical S-adenosylmethionine enzyme PqqE shown here. **(d)** A comparison of Nuclear Quadrupole Resonance (NQR) signal strengths as a function of standoff distance from an explosive sample shows that the signal enhancement techniques developed by the author (red) greatly outperform traditional detection methods (black).

Table 1. The magnetic resonance properties of these selected actinide nuclei are markedly different from those of hydrogen-1 and nitrogen-14 , the most common target nuclei in NMR and NQR, respectively. They typically have low gyromagnetic ratios, high quadrupole moments, and large nuclear spins. Data reproduced from the EasySpin nuclear isotope database (easyspin.org).

Element	Isotope	Spin	Gyromagnetic ratio (γ), MHz/T	Quadrupole moment (Q), milliBarn	Natural abundance, %
1 Hydrogen	1	½	42.6		100
7 Nitrogen	14	1	3.1	20	100
89 Actinium	227	3/2	5.6	1700	0
90 Thorium	229	5/2	1.4	4300	0
	232				100
91 Protactinium	231	3/2	5.1	1720	100
92 Uranium	234				<<1
	235	7/2	–0.8	4936	1
	238				99
93 Neptunium	237	5/2	9.6	3870	0
94 Plutonium	239	½	3.1		0
95 Americium	241	5/2			0
	243	5/2	4.6	2860	0
96 Curium	247	9/2	0.3		0

High-field NMR

Given the challenges presented by actinide nuclei highlighted above, work realizing the potential of MR in actinide science has been slow. Initial attempts have all been made in traditional high-field NMR systems. Despite their high costs, cryogenic temperature requirements, size, and weight, such systems are used because the strong static magnetic field, tens of thousands of times the Earth's magnetic field, produces larger signals. The first observation of uranium-235 was performed in 1983 by Le Bail and co-workers with such a system. Similarly, plutonium-239's signal was first observed in an NMR system by Yasuoka and co-workers in 2012 with a measurement made at LANL using a high-field instrument with a solid sample of PuO_2 at 4 K (to read more about this, see ARQ Issue 2, 2013). This team had to painstakingly search for the NMR signal by incrementally varying the magnetic field of their magnet since they did not know the gyromagnetic ratio of the nuclei. Their results, including the first measurement of the nuclear gyromagnetic ratio of plutonium-239, pave the way for future research in this arena.

Low-field NMR

To extend this work, current researchers at LANL are developing a low-field NMR system to target plutonium. By working with a static field only tens of times larger than Earth's field, the frequency of the NMR signal will be sensitive to structural information encoded by the sample and should give the exact identity of metal speciation and actinide chemistries. A portable low-field device could provide rapid measurements to help decision making in areas of environmental management and non-proliferation. Since the NMR signal decreases rapidly with decreasing static field strength, this system incorporates dynamic nuclear polarization, a technique that combines the physics of EPR with NMR, to enhance the signal of the target nuclei by several orders of magnitude. Essentially, the system uses the unpaired electrons in an intermediate compound mixed with the target compound as a means to efficiently excite the target nucleus. The LANL system has successfully observed signals using increasingly heavier and more demanding nuclei. Unfortunately, it is challenging to direct the unpaired electrons to excite specific nuclei in this technique—this is being addressed in current work focused on controlling the interaction of the electrons to force them to excite only the target nuclei.

NMR with no applied field

An interesting NMR observation of uranium-235 was performed by Ikushima et al. in 1998. While uranium-235 has an exceptionally high quadrupole moment, the researchers were able to observe an NMR signal by working with no applied field (Fig. 3). As the ^{235}U-enriched uranium dioxide (f^2) sample was cooled below 4 K, the magnetic moment of the sample's electrons provided a hyperfine field across the uranium nuclei. This field was measured as 252 T—for comparison, the Earth's magnetic field is roughly 50 μT, meaning the uranium nuclei were experiencing an extremely localized magnetic field over five million times the strength of Earth's field. This leads the way to additional measurements on actinide compounds, since similar predicted field strengths have been reported for neptunium and americium compounds, making observation of those nuclei also within reach.

Nuclear Quadrupole Resonance

Given the large quadrupole moment of many of the actinide nuclei, one of the most promising investigative tools is NQR; however, successful measurements have yet to be performed. Unlike in NMR, no static magnetic field is necessary, and the large quadrupole moment is actually beneficial in NQR—the larger the quadrupole moment, the easier it is to detect the species. In principle, observing NQR signals of actinides should be straightforward, but there are many issues to be resolved before such an observation is obtained. In contrast to NMR and MRI, the NQR frequencies of compounds are not controlled by the experimentalist. In those techniques, the frequency is given by the product of the target's gyromagnetic ratio and the applied static magnetic field. While some consideration must be given to the local magnetic fields near the nuclei, localized fields are rarely as extreme as the 252 T described above. In contrast, for NQR the frequencies are unknown until they are found. While tools to predict NQR frequencies can provide a search region, confirmation via experimental measurements can be extremely time intensive as each frequency range must be laboriously tested to isolate the NQR signature from background noise.

»» A **hyperfine field** *is a magnetic field created by electrons orbiting the nucleus of an atom. In effect, it is a magnetic field that is created internally by a material and can create secondary effects on peaks in the spectra.*

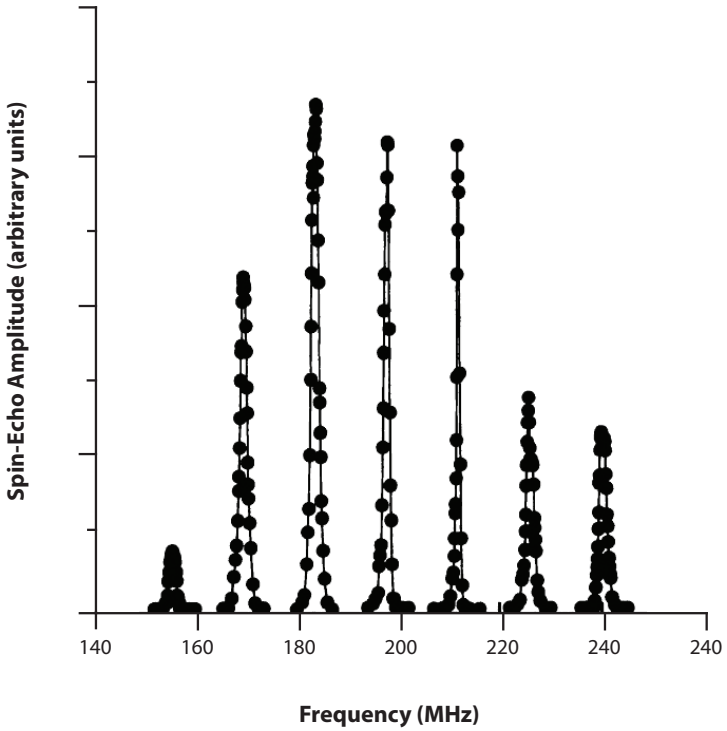

Figure 3. This data shows a ^{235}U NMR signal obtained in the absence of applied field. This was observed in $^{235}UO_2$ due to the 252 T hyperfine field from neighboring electrons, which could only be observed below 15 K. The rapid decay of the signal further increases the difficulty in observing such signals—these types of experimental challenges slow the development of magnetic resonance for actinide science. The seven resonance lines are a consequence of uranium-235's large spin.

The most powerful tool for predicting NQR frequencies is density functional theory (DFT), which can be used to predict the electric field gradient given a known chemical and crystal structure. While DFT has been successfully used to predict NQR frequencies for heavy nuclei such as gold (atomic number; *Z;* number of protons in the nucleus = 79), current methods for DFT appear unsuitable for 5f-elements such as uranium-235 ($Z = 92$). In part, this is due to the complexity that relativistic effects introduce into the calculations for such heavy nuclei. Since the electron binding energy is proportional to Z squared, heavy atoms have increasingly larger binding energies. Eventually the binding energy of the core electrons becomes comparable to the rest mass of the electron, and this motivates the need for relativistic corrections in the DFT calculation, greatly increasing the computational complexity of the calculation. While DFT can generate a result, the uncertainties currently span orders of magnitude from MHz frequencies and up, making attempts at experimentally confirming actinide NQR frequencies extremely slow and costly due to the large amount of specialized equipment it would require.

Summary

The incremental advances in magnetic resonance studies of actinides reflect the number of challenges these materials present both theoretically and experimentally. Non-destructive, standoff interrogation techniques such as NMR and NQR, while still requiring a significant investment to bring them to fruition, show many potential benefits, and interest in the topic is growing, with LANL well positioned to be a leader in this area.

Further reading:

1. *H. Le Bail, C. Chachaty, P. Rigny, and R. Bougon, "Observation of the Uranium-235 Nuclear Magnetic Resonance Signal", J. Phys. Lett-Paris, 1983, 44 (24), 1017–1019.*
2. *H. Yasuoka, G. Koutroulakis, H. Chudo, S. Richmond, D. K. Veirs, A. I. Smith, E. D. Bauer, J. D. Thompson, G. D. Jarvinen, and D. L. Clark, "Observation of 239-Pu Nuclear Magnetic Resonance", Science, 2012, 336 (6083), 901–4.*
3. *K. Ikushima, H. Yasuoka, S. Tsutsui, M. Saeki, S. Nasu, and M. Date, "Observation of 235-U NMR in the Antiferromagnetic State of UO_2", J. Phys. Soc. Jpn., 1998, 67 (1), 65–66.*

Toward High-Precision Plutonium Density Measurements: Investigating Errors in Measuring Self-Heating Samples

Alexandria Marchi

Alexandria Marchi was a Seaborg fellow from October 2015 to December 2016, mentored by David Mascarenas and Albert Migliori. Her area of interest was materials engineering. She is now an R&D scientist in the Materials Synthesis and Integrated Devices group (MPA-11).

Understanding the state and aging of plutonium is essential for monitoring the nation's nuclear stockpile. This can be challenging, however, as complex microstructural changes occur because of the poorly understood transitions between its six different solid phases, which are accompanied by large density changes. Complicated radiological decay and variations in metallurgical processing techniques lead to samples with varying phase compositions, quantifiable in part by precise density measurements. Therefore, these measurements are important for studying the dynamic properties of plutonium. They require an accurate method of measuring a sample's volume—at Los Alamos National Laboratory (LANL), this is typically performed using hydrostatic immersion techniques based on Archimedes' Principle, where volume is determined by the buoyancy force applied by an immersion fluid. This force, in turn, is largely determined by the fluid's temperature-dependent physiochemical properties.

Density measurements of plutonium are significantly complicated by the fact that it is a very dense, highly reactive, self-heating material (to illustrate this, the latter property is used in thermoelectric Pu batteries for space exploration). These characteristics result in multifaceted interactions (chemical, physical, and radiological) with the immersion fluid, leading to imprecise measurements. This article addresses how the self-heating nature of plutonium increases the uncertainty of the measurement that, if not correctly accounted for, will decrease its accuracy. Self-heating effects were analyzed by modeling the change in buoyancy force under convective flow patterns present during density measurements of samples while considering different fluid properties, sample geometries, and sample heat outputs. Ongoing work aims to validate these models using machined tungsten-alloy samples with integrated surface-mount resistors to emulate self-heating combined with diagnostic techniques, e.g., high-precision balance measurements and Schlieren flow visualization.

Immersion fluids in use

Plutonium density measurements occurred as early as 1954 with Laquer, who reported difficulties and gave an accompanying error analysis, noting the convection effects on measurements in bromobenzene. However, without the computational capabilities of the modern age, calculating the magnitude of the effects from convective currents was not possible. Density measurements have continued at various laboratories within the Department of Energy (DOE) nuclear complex without quantification of these effects.

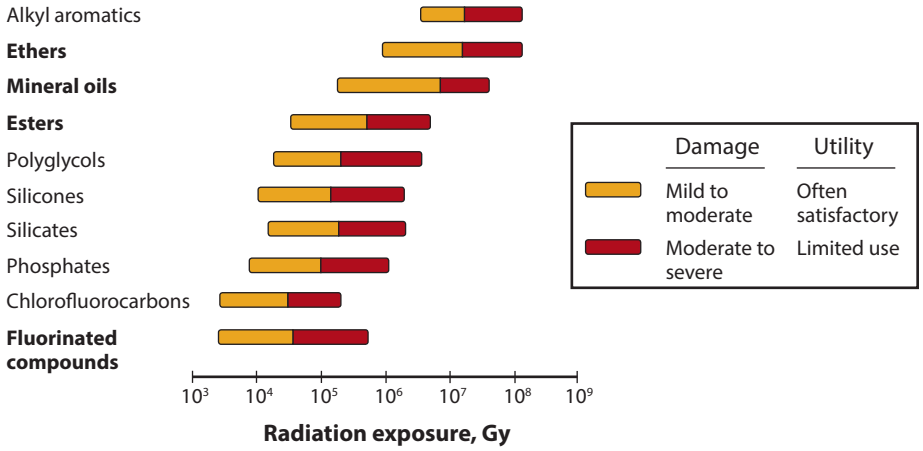

Figure 1. Radiation resistance of base oils shows improved resistance of ethers, mineral oils, and esters over the currently used fluorinated compounds (taken from "Safe Handling of Tritium Review of Data and Experience", IAEA,1991).

Around 2006, perfluorotributylamine (FC-43), a fluorocarbon-based fluid, replaced bromobenzene as an immersion fluid. The high density of this fluid increased the sensitivity of the measurements, which has been used at both Lawrence Livermore National Laboratory and Rocky Flats. However, other materials were not fully considered when this new fluid was adopted. Fluorinated compounds have low radiation resistance (compared to other basic oils), do not transfer heat well, evaporate rapidly, and are expensive to purchase and dispose of because of high environmental hazards. This work aims to identify potential replacement immersion fluids based on their chemical reactivity, corrosion potential, thermomechanical properties, radiation resistance, and aging characteristics in the presence of Pu.

Choice of surrogate fluids

Potential fluid types were identified based on a report detailing radiation resistance among different oil types ("Safe Handling of Tritium Review of Data and Experience", published by the International Atomic Energy Agency in 1991; data illustrated in Fig. 1). Accordingly, attention was focused on ethers, mineral oils, and esters as they show increased radiation resistance over currently utilized fluorinated compounds. Low-viscosity properties are also critical because wetting properties are crucial for high-precision measurements. Fluorinated compounds have a relatively high vapor pressure, leading to fluid evaporation and evaporative cooling, causing convective surface forces on the sample during measurement. Therefore, a lower vapor pressure is desired. As plutonium is inherently self-heating, the fluid's thermal coefficient of expansion will affect the fluid's density.

The density profile surrounding the sample is a function of the fluid's thermal conductivity, heat capacity, viscosity, and coefficient of expansion. A clear understanding of this profile and how these values influence the surface forces on the sample will aid in determining a potential immersion fluid surrogate.

Physiochemical property data for all potential fluids do not currently exist; therefore, only fluorocarbon fluids were simulated. Table 1 lists the properties of water and fluorocarbon fluids; also shown are sample geometries and orientations that were chosen to simulate.

Modeling self-heating effects

Convective flow around the self-heating sample reduces the precision of Pu density measurements in part due to the effects of density gradients in the immersion fluid. These gradients and the resulting surface forces vary based on fluid properties, sample geometry, and initial system environment. Computational models can

Properties at 298 K	Immersion Fluids					
	Water	FC-43	FC-72	FC-75	Novec 7500	Novec 7700
Density, kg/m^3	998	1859	1675	1764	1614	1797
Coefficient of Thermal Expansion, K^{-1}	3.1×10^{-4}	1.2×10^{-3}	1.6×10^{-3}	1.4×10^{-3}	1.3×10^{-3}	1.1×10^{-3}
Dynamic Viscosity, Pa·s	8.9×10^{-4}	5.3×10^{-3}	6.9×10^{-4}	1.5×10^{-3}	1.2×10^{-3}	4.4×10^{-3}
Thermal Conductivity, W/m·K	6.0×10^{-1}	6.5×10^{-2}	5.8×10^{-2}	6.3×10^{-2}	6.5×10^{-2}	6.5×10^{-2}
Heat Capacity, J/kg·K	4183	1053	1045	1025	1028	1025
Sample Geometries						

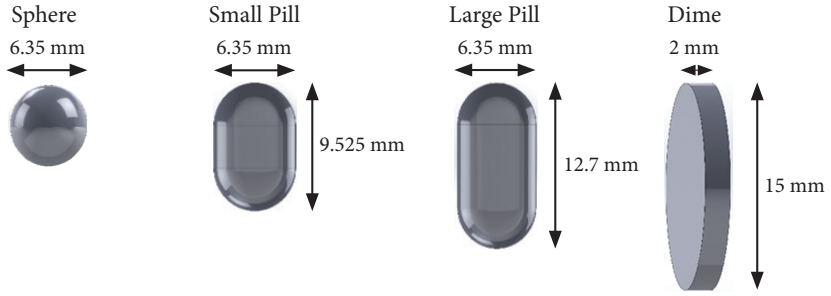

Table 1. Property data for modeled potential surrogates and sample geometries. For the simulations, each sample geometry was immersed in fluid in its vertical orientation (as shown), while the dime sample was simulated in the vertical and horizontal orientations (rotated 90° about the axis normal to the page). Fluid data was provided by the manufacturer 3M for the fluorocarbon fluids or through COMSOL's fluid property database, which is taken from the JAHM Software, Inc. material properties database (*www.jahm.com*), for water.

expedite experimental studies by rapidly quantifying immersion fluid effects on Pu density measurements. The immersion fluid properties affect the fluid dynamics around and resulting buoyancy forces on the sample. The time to achieving a steady state and plume shape also varies based on the fluid's properties, sample geometry, and heat output. Therefore, a set of immersion fluids and sample geometries was modeled to determine differences in time to steady state and changes in buoyancy forces over time from the start of sample heating. Sample self-heating initiates free convective flow around the sample, which produces density gradients and fluid flow-inducing changes in the pressure and shear forces on the sample. Modeling this problem to the desired precision (goal of measurement precision 10^{-4}–10^{-6} g on < 10 g samples) is challenging because the temperature dependence of fluid property values must be taken into account. Therefore, the relationship between heat transfer and fluid flow must be captured while considering compressible flow. The simulation software COMSOL Multiphysics® 5.2 was chosen to model this free convective flow with variable material properties.

Sample geometry and orientation

The geometry of the sample affects the convective flow profile and resulting buoyancy force in multiple ways, as 1) power output (from self-heating) depends on sample volume and 2) free convection causes upward flow due to gravity, which produces viscous forces along sample corners, faces, edges, and surface ridges. Four sample geometries were chosen based on ease of machining tungsten mimics and common Pu sample shapes used for density measurements: spherical, large pill, small pill, and dime (see images in Table 1). The latter three geometries were oriented vertically and horizontally to assess the effects of sample orientation.

Sample geometry also plays a clear role in both the shape and time for equilibration of a boundary layer around the sample. Upon initial heating, conductive heat transfer dominates, producing symmetrical gradients about the object. After

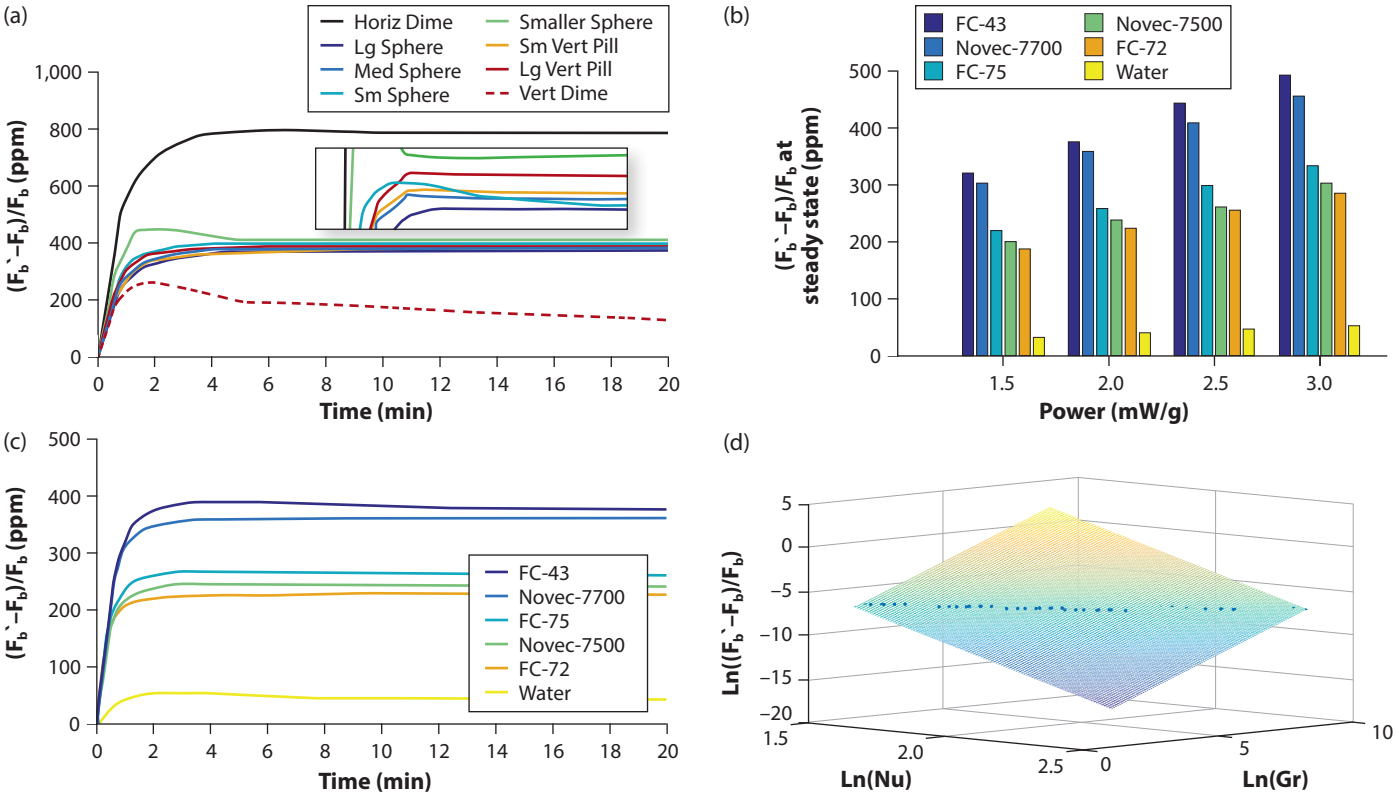

Figure 2. Data from COMSOL simulations: **(a)** This plot shows that the sample's geometry and orientation have a definitive effect on the forces on the sample; **(b)** This graph shows that changes in the forces on the sample increase linearly with increasing power; **(c)** This data shows that different fluids produce different changes in the forces on the sample, with water showing the least significant change; **(d)** The dimensionless correlation fit to simulation data for the fluorocarbon fluids around a sphere with varying heat loads shows that the thermal conductivity seems to be the most important thermophysical property to minimize the uncertainty in the volume measurement of the sample because of convective flow. Gr = Grashof number, and Nu = Nusselt number. $(F_b'\text{-}F_b/F_b)$ is the uncertainty in the buoyancy force on the sample if heating is not considered; i.e., F_b' is the buoyancy force with the self-heating object, and F_b is the buoyancy force without heating.

some time (dependent on the sample size and shape), viscous forces emerge in which convection produces upward shearing on the sample. The ratio between buoyancy and viscous forces depends on the fluid's properties, characteristic length of the sample, and the temperature difference between the surface of the sample and the bulk fluid, as described by the Grashof number (Gr). By holding the heating rate and fluid constant, the effects of different sample geometries can be explored.

The samples that exhibited the greatest initial change in force upon heat load were the horizontally placed geometries. The large difference in behavior of the large pill between its vertical and horizontal orientation, and the small difference in behavior between the vertical large pill and the vertical small pill and sphere provide strong evidence that the orientation of the sample based on its aspect ratio will provide different density measurement results. Fig. 2a shows an example plot of the variation in sample forces based on sample geometry in FC-43. These qualitative results will help determine how samples should be oriented during density measurements to minimize the effect on changes in the buoyancy force on the sample from convection.

Self-heating sample power output

The heat load from Pu is typically low, around 2–5 mW/g, depending on the sample age and isotopic composition, including the quantity of americium (which is formed from radioactive decay of plutonium). Simulations showed that changes to the forces on the sample increase sharply initially and then equilibrate to a steady state. These transient behaviors generally emulate an underdamped system that is dependent on heat load. Typically, these small samples and low heat loads reach a steady state after 10 minutes. The force difference appears to be linear with time in most cases, with the slope dependent on the fluid and geometry, suggesting a proportional relationship between heat output and the heat-induced buoyancy force on the

sample. The Nusselt number best characterizes the temperature gradient along the sample's surface based on the heat load. Fig. 2b shows an example plot of a sphere in each fluid with increasing heat load. This information will help with density measurements of samples with unknown heat loads.

Immersion fluid property effects

The collection of fluids studied in this work encompasses a large range of thermomechanical property values, from water to oils. In all geometries and with all power sources, the time to steady-state can be ranked as follows: water < Novec-7700 < FC-43 < FC-72 (Fig. 2c). Looking at each of their relevant thermophysical properties (Table 1), it is not obvious which property plays the most important role in reducing the variation in buoyancy forces on the sample. In order to inform our choice of fluid we can correlate the Prandtl number (Pr), which gives the ratio of the momentum and thermal diffusivities, Grashof number (Gr), which describes the temperature difference between the surface of the sample and the bulk fluid, and Nusselt number (Nu), which is the dimensionless temperature gradient at the sample's surface. In order to correlate the large quantity of data for the various test cases, dimensional analysis was used to determine the relationship between the buoyancy forces on the sample and the various fluid properties and heat outputs from the sample. Simulation data was fit to a dimensionless equation that relates the buoyancy force on the sample to the physical properties of the immersion fluid. Results from this correlation (Fig. 2d) show that the fluid's thermal conductivity and thermal coefficient of expansion predominately affect the convection-driven buoyancy force on the sample. This outcome guides immersion fluid selection criteria.

Experimental flow visualization

Many flow imaging techniques have evolved to generate quantitative data on complex flow problems. One such technique, Schlieren flow visualization, was first documented in the 17th century by Robert Hooke in his famous Micrographia book, documenting many significant observations with lenses. While originally used as a qualitative measurement of gas flow, Schlieren techniques have also been employed for visualizing liquid flow. This technique produces a pattern of light and dark

«« **Dimensional analysis** *is a problem-solving tool which analyzes the relationships between different physical quantities by identifying their base quantities and units. It lowers the number of variables in a fluid phenomenon by mixing some variables to form parameters which have no dimensions, and therefore simplifies the equations.*

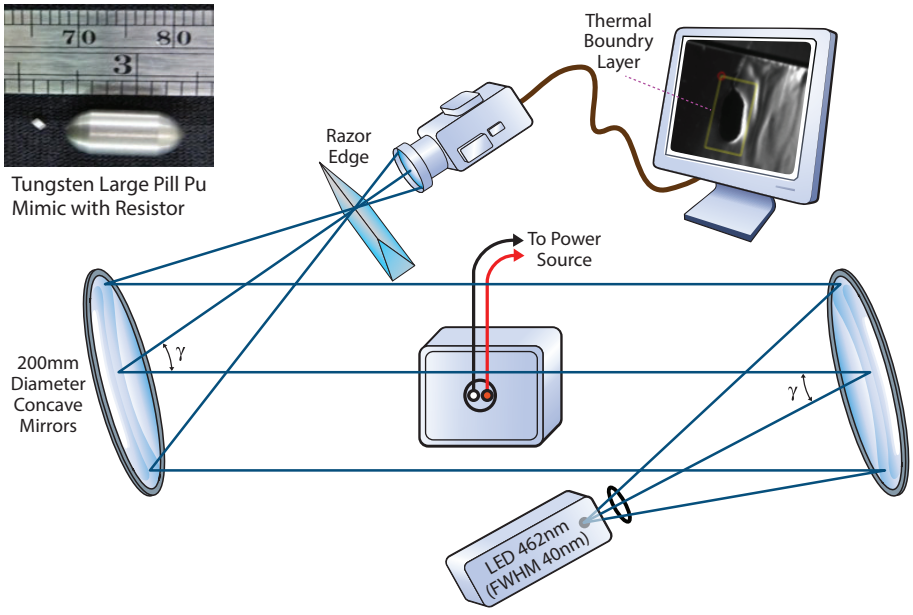

Figure 3. Schematic of setup for Schlieren flow visualization studies. The sample is heated and weighed while hanging from a balance to characterize mass changes as a function of density changes, and viscous forces in the fluid as quantified from Schlieren visualization.

contours caused by the deflection of light rays through a density gradient (Schlieren object). Recently, a number of techniques have been used to quantify Schlieren effects in fluids, e.g., using calibration lenses and focus filaments.

Currently in its initial development stages, Fig. 3 shows the Schlieren method setup. A machined tungsten alloy pill-shaped sample embedded with a surface mount resistor (1–15 kΩ) was hung from the bottom of a high-precision balance (Mettler Toledo XP6U) using the wires supplying current to the resistor through a sourcemeter. Upon initiating the current, a thermal boundary layer developed, which was qualitatively consistent with the computational simulations in its overall shape. The thicker boundary layer was more easily visualized in the FC fluids than in water due to their larger coefficients of thermal expansion. However, FC fluids are disadvantaged by absorbing large amounts of oxygen and possessing high evaporation rates. The high evaporation rates led to what appeared to be evaporative cooling-induced convection cells, traditionally described as Rayleigh-Bénard convection. These effects, though not entirely resolved, produce flow patterns in the fluid which disrupt the mass measurements. Rayleigh numbers for each fluid will need to be calculated to determine the effect of Rayleigh-Bénard convection for each fluid type, which could impact fluid choice. Unfortunately, large and currently unexplained variations in mass measurements have delayed full data analysis. In this ongoing work we are striving to improve data collection, develop a more stable fluid environment, and apply quantitative techniques.

Summary

To date, this work has focused on analyzing commercially-available immersion fluid surrogates and simulating the forces on a self-heating object of various geometries in multiple fluids. The simulations show great dependence on the sample orientation, fluid properties, and power output from the sample. Determination of a dimensionless correlation has guided immersion fluid selection. Initial flow visualization studies have shown promise in sensitivity in which the thermal boundary is visible with this technique. Future work in this area will include the development of a quantitative technique coupled with sensitive balance measurements. Ultimately, definitions to qualify an immersion fluid will be established such that the most appropriate fluid choice can be made to improve the accuracy of density measurements for Pu and related materials.

Acknowledgments

The author gratefully acknowledges the a Glenn T. Seaborg Institute Fellowship, and is thankful for support from Albert Migliori, Franz Freibert, Scott Richmond, Dave Reagor, and Dave Clark for numerous discussions and guidance in all things plutonium; Robert Morgan and other AET-1 staff for their diagnostic support; Hannah Worrest for helping with the COMSOL simulations and setting up the Schlieren workspace; Andrew Dattelbaum and Jeffrey Willis for helping get the laboratory up and running in MPA-11; Kirk Hollis and Jon Rau for discussions regarding fluid aging and radiation damage; Ellie Vigil and Susan Ramsay for their unfailing efforts in administrative support. The author also acknowledges the LDRD program for funding the "Aging in delta-Pu Alloys" (project #20150057DR), whose members provided significant guidance throughout this project's tenure, and the current program management of the Weapons Safety and Surety and Plutonium Sustainment Programs for continuing to support these efforts.

Further reading:

1. *H. L. Laquer, "The Density of Alpha-phase Plutonium," Chem. Elem., vol. LA-1656, 1954.*
2. *International Atomic Energy Agency, "Safe Handling of Tritium Review of Data and Experience", Technical Reports Series No. 324, IAEA, Vienna (1991).*
3. *W. G. Wolfer, A. Kubota, P. Söderlind, A. I. Landa, B. Oudot, B. Sadigh, J. B. Sturgeon, and M. P. Surh, "Density changes in Ga-stabilized δ-Pu, and what they mean", J. Alloys Compd., 2007, 444–445, 72–79.*
4. *K. M. Dziewinska, A. M. Peters, J. A. Laverne, P. Martinez, J. J. Dziewinski, L. B. Davenhall, and P. Rajesh, "In search of an optimum plutonium density measurement fluid", Radiochim. Acta, 2009, 97, 4–5, 213–217.*
5. *A. Marchi, R. Morgan, H. Worrest, J. Bernardin, and F. Freibert, "Simulation and Experimental Validation of the Thermal Influence on Self-Heating Metal Density Measurements", ASME. Heat Transfer Summer Conference, 2017, 2; doi:10.1115/HT2017-4992.*

Actinide Detection Using Photoluminescence: Resonant Non-Radiative Energy Transfer Between Actinyl Ions

Detection of actinide elements in trace quantities is of great importance to national security, nuclear nonproliferation, and waste handling. It can be a challenging task—for instance, detection of neptunium is difficult using nuclear counting methods. Detection methods based on photoluminescence meanwhile have the potential to be highly sensitive and selective for a given chemical species. One major problem is that many actinide molecules suffer from low quantum yields, making detection by photoluminescence difficult.

One strategy that can be employed to enhance photoluminescence from actinides is to use resonant non-radiative energy transfer (RNET) from a host material to the analyte. Here, the analyte is incorporated into a matrix material which strongly absorbs light. If several conditions are met, fast and efficient energy transfer from the matrix material to the analyte can occur. This transfer of energy could enhance photoluminescence from the analyte of interest—this is because light can be absorbed by the more abundant matrix material, which then transfers its energy to the analyte.

Resonant non-radiative energy transfer, often called fluorescence resonance energy transfer (FRET), is a phenomenon that has been exploited in a wide array of fields, including solar cell conversion and laser development, and is used in molecular biochemistry to probe conformational changes in large proteins. RNET in the solid state between two different actinide ions has not been previously reported, however it has been studied between uranyl (UO_2^{2+}) and lanthanide ions. Studies in which uranyl ions are co-doped with lanthanide ions in a glass matrix have shown that RNET can be very efficient, nearing 100% of the energy transferred from the uranyl ion to the lanthanide. Here, the first observation of RNET between two different actinide ions in the solid state is presented. This was accomplished by analyzing the photophysical dynamics in $Cs_2UO_2Cl_4$ crystals doped with small quantities of $Cs_2NpO_2Cl_4$ using time-resolved photoluminescence spectroscopy. With RNET, we were able to use photoluminescence to detect concentrations of $Cs_2NpO_2Cl_4$ that were lower than we previously thought possible.

Target species

Experimental photoluminescence measurements of structurally symmetric and electronically simpler complexes can serve as models for the development of detection capabilities for real world actinide complexes. Actinyl species, in particular UO_2^{2+}, NpO_2^{2+}, and PuO_2^{2+}, are attractive targets for study because they contain only a few unpaired 5f metal-centered valence electrons (f^0, f^1, and f^2, respectively), which results in simpler spectra that can be quantitatively analyzed. While the closed shell f^0 uranyl ion has been previously studied in detail, the complexity of the open-shell

Beau J. Barker

Beau Barker was a Seaborg Postdoctoral Fellow from 2012 to 2014 and was mentored by Marianne Wilkerson and John Berg. His Seaborg work focused on spectroscopy and resonant non-radiative energy transfer in actinyl ions. He now works as a scientist in the Analytical Laboratory located in the Materials and Fuels Complex at Idaho National Laboratory, where he focuses largely on isotopic and elemental analysis of irradiated nuclear fuels.

Acknowledgments

This material is based upon work supported by the U.S. Department of Energy, Office of Science, Office of Basic Energy Sciences and the LANL LDRD program. The author is also grateful to Stosh Kozimor and Iain May for the synthesis of the crystals used in this study as well as Marianne Wilkerson and John Berg whose insights and mentorship made this work possible.

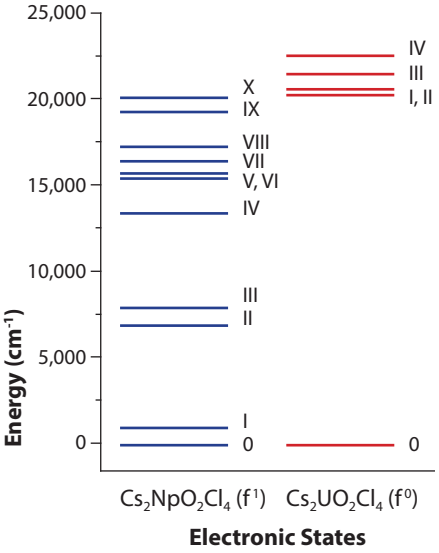

Figure 1. Energy level diagram for the low-lying electronic states of $Cs_2NpO_2Cl_4$ (blue) and $Cs_2UO_2Cl_4$ (red).

systems has made characterization of neptunyl and plutonyl species more difficult.

Fig. 1 shows an energy level diagram for the low-lying electronic states of $Cs_2NpO_2Cl_4$ and $Cs_2UO_2Cl_4$. The open-shell f^1 species, $Cs_2NpO_2Cl_4$ has a rich spectrum in the near-IR and visible range (approximately 4,000–25,000 cm^{-1} or 400–2,500 nm), and has strong photoluminescence only in the near-IR (4,000–12,500 cm^{-1} or 800–2,500 nm). This contrasts with the closed-shell f^0 species $Cs_2UO_2Cl_4$, whose lowest-energy electronically excited state is at ~20,000 cm^{-1} (500 nm), giving a large window in which the host is optically transparent. This allows the study of the electronic structure and photophysical dynamics of the $Cs_2NpO_2Cl_4$ dopant. The $Cs_2UO_2Cl_4$ host matrix was also chosen because its crystal structure is nearly identical to that of pure $Cs_2NpO_2Cl_4$, which facilitates the formation of crystals of the doped system.

Spectroscopic methods

We recorded excitation and emission spectra, in addition to time-resolved photoluminescence waveforms, for pure $Cs_2UO_2Cl_4$ crystals and $Cs_2UO_2Cl_4$ doped with small amounts of $Cs_2NpO_2Cl_4$; the doped system is referred to as $Cs_2U(Np)O_2Cl_4$. To record an excitation spectrum, the photoluminescence from a particular emission band belonging to the molecule of interest is monitored while scanning the excitation source, in our case a tunable laser. In principle, an excitation spectrum gives information equivalent to an absorption spectrum. If a molecule has strong photoluminescence, then recording an excitation spectrum has the advantage that sensitivity can be greater than the corresponding absorption spectrum, particularly for samples with small path lengths, such as single crystals.

To record an emission spectrum, the excitation source is fixed at the energy of a known electronically excited state, and the resulting photoluminescence is dispersed through a monochromator and scanned. While emission between excited electronic states is possible, typically the detected luminescence is between one or more electronically excited states and the ground electronic state. In time-resolved photoluminescence, luminescence from an excited electronic state is observed as a function of time. From this, the lifetime of the excited electronic state can be found in addition to the possibility of coupling between the monitored electronic transition and any higher-lying excited electronic states.

Energy transfer by RNET

In RNET, no real photons are emitted or absorbed. Instead, the sensitizer in an electronically excited state transfers its energy by inducing a multipole-multipole interaction (for example a dipole-dipole) on a nearby acceptor; in our study, the $Cs_2UO_2Cl_4$ matrix is the sensitizer and the $Cs_2NpO_2Cl_4$ dopant is the acceptor. This contrasts with resonant radiative energy transfer in which energy transfer occurs by photon emission from the sensitizer, which is then adsorbed by an acceptor.

The probability of RNET occurring between two molecules depends on several factors, the most important being the distance between the sensitizer and acceptor, in addition to the spectral overlap between the sensitizer and acceptor (the spectral overlap is defined as the overlap between the absorption or excitation spectrum of the acceptor and emission spectrum of the sensitizer). RNET also depends on the quantum efficiency and photoluminescence lifetime of the sensitizer. Fig. 2 describes a simplified outline of the energy transfer process.

The crystal structures of both $Cs_2NpO_2Cl_4$ and $Cs_2UO_2Cl_4$ are known—the

shortest metal-metal distance is ~5.8 Å, which is sufficiently close for RNET to occur (RNET has been known to occur at distances greater than 50 Å). There is also good spectral overlap between the excitation (absorption) spectrum of $Cs_2NpO_2Cl_4$ and the emission spectrum of $Cs_2UO_2Cl_4$, shown in Fig. 3a. Finally, uranyl species are known to have a high quantum efficiency and relatively long lifetimes. The pure $Cs_2UO_2Cl_4$ crystals used in this study have a photoluminescence lifetime of ~1000 µs at 77 K. Therefore, the $Cs_2U(Np)O_2Cl_4$ doped system meets the above criteria for efficient RNET to occur.

Initial discovery of energy transfer in $Cs_2U(Np)O_2Cl_4$ crystals

Energy transfer between uranyl and neptunyl was initially observed in 3% doped $Cs_2U(Np)O_2Cl_4$ crystals at liquid nitrogen temperature while attempting to collect an excitation spectrum of the $Cs_2NpO_2Cl_4$ dopant at energies greater than 20,000 cm^{-1} (500 nm). Starting at this energy, features belonging to the $Cs_2UO_2Cl_4$ matrix dominated the excitation spectrum. This result was unexpected because the excitation spectrum was recorded by monitoring photoluminescence belonging only to the $Cs_2NpO_2Cl_4$ dopant and an excitation spectrum of the dopant should have been obtained. Fig. 3b compares the excitation spectrum of 3% doped $Cs_2U(Np)O_2Cl_4$ crystals collected while monitoring near-IR photoluminescence from the II → 0 transition (at 6880 cm^{-1} or 1453 nm) of the $Cs_2NpO_2Cl_4$ dopant, along with an excitation spectrum of pure $Cs_2UO_2Cl_4$. As shown in Fig. 3b, we could only detect features which belonged to the uranyl host above 20,000 cm^{-1} (recall from Fig. 1 that this is the energy of the first excited electronic state of the uranyl matrix). This was a surprising result, given that $Cs_2UO_2Cl_4$ does not luminescence where the detector was tuned. This led us to hypothesize that the uranyl host absorbs a large portion of the excitation energy and then transfers it to neptunyl dopant so efficiently that features belonging to the uranyl host dominate the excitation spectrum of the doped system above 20,000 cm^{-1} (500 nm) in energy.

Time-resolved photoluminescence spectra and confirmation of the RNET mechanism

To test this hypothesis, and to determine the type (radiative or RNET) and rate of energy transfer, time-resolved photoluminescence data for both uranyl and neptunyl were collected as a function of excitation energy for crystals with neptunyl doping levels in the range 0–5%. The radiative mechanism could be easily ruled out because the photoluminescence lifetime and intensity of emission from the uranyl host quickly decreased with increasing neptunyl concentration, from 1000 µs in the pure crystal to ~3 µs in a 1% crystal. If energy was transferred by a radiative mechanism, the lifetime of the host would not depend on dopant concentration.

It was found that the time-resolved photoluminescence waveforms varied

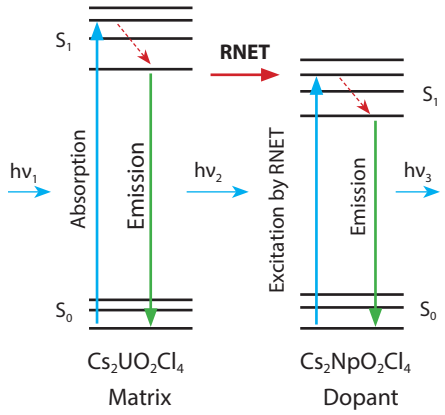

Figure 2. Simplified outline of the energy transfer process. First, the sensitizer absorbs an incoming photon (labeled $hν_1$) and excites it into an electronically excited state denoted as S_1 (S_o is the ground electronic state). At this point, the sensitizer can either return to the ground electronic state by emitting a photon ($hν_2$) or it can transfer its energy to a nearby acceptor molecule via RNET; these two processes (radiative and non-radiative) directly compete. If the energy is transferred to the acceptor, then the acceptor is excited into an electronically excited state (S_1) and can return to the ground electronic state (S_o) by emitting a photon ($hν_3$).

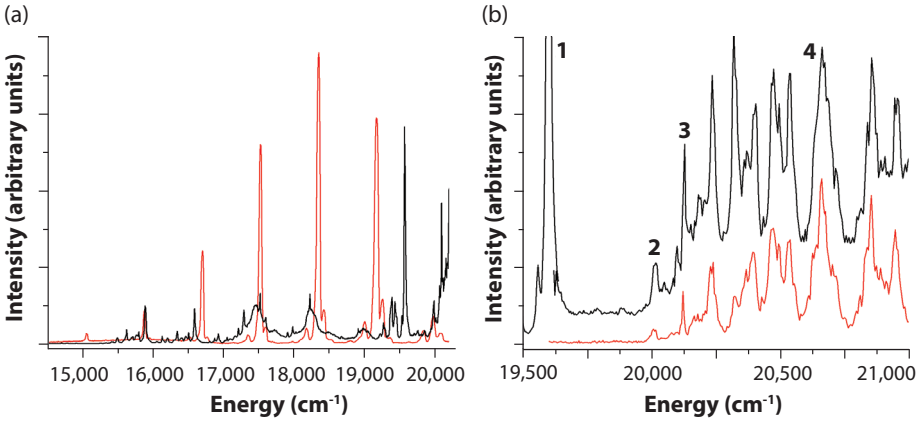

Figure 3. **(a)** Excitation spectrum of $Cs_2NpO_2Cl_4$ (black trace) overlaid with the emission spectrum $Cs_2UO_2Cl_4$ (red trace). Good spectral overlap is required for RNET to occur. **(b)** Excitation spectra of $Cs_2U(Np)O_2Cl_4$ (black trace), and pure $Cs_2UO_2Cl_4$ (red trace). Note the similarity in the region above 20,000 cm^{-1} (500 nm), which was the first indication that RNET was occurring. Labeled peaks show the following transitions: **1**. Neptunyl IX + $ν_{3/6}$ **2**. Uranyl 0 + $ν_{8/9}$ **3**. Uranyl I,II (origin) **4**. Uranyl III (see Fig. 1 for reference).

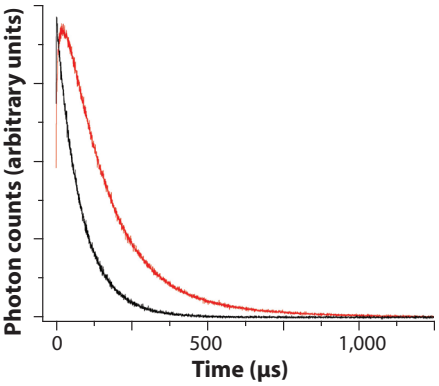

Figure 4. Time-resolved photoluminescence waveforms recorded while monitoring $Cs_2NpO_2Cl_4$ photoluminescence from the II → 0 transition at 6880 cm^{-1} (1453 nm) in a crystal containing 0.3% $Cs_2NpO_2Cl_4$ at liquid nitrogen temperature. The "in-growth" feature in the red trace (recorded while pumping a $Cs_2UO_2Cl_4$ transition above 20,000 cm^{-1}) is due to RNET, while the black trace (recorded while pumping a $Cs_2NpO_2Cl_4$ transition below 20,000 cm^{-1}) shows normal radiative emission for comparison.

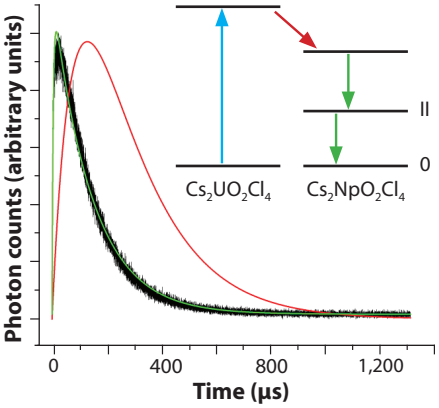

Figure 5. The results of two kinetic models for energy transfer. The red trace assumes only radiative transfer and the green trace includes RNET. The black trace is the experimental data.

depending on the excitation energy, which gives further insight into the energy transfer mechanism. Fig. 4 shows the time-resolved photoluminescence waveforms from the $Cs_2NpO_2Cl_4$ II → 0 transition at 6880 cm^{-1} (1453 nm) for two different excitation energies. The black trace was recorded using an excitation energy below 20,000 cm^{-1} (500 nm) and represents normal radiative photoluminescence emission in the absence of RNET. This waveform can be used to determine the lifetime of the $Cs_2NpO_2Cl_4$ II → 0 transition (~100 μs at 77 K). The red trace was recorded while pumping a uranyl transition above 20,000 cm^{-1}. It shows an initial rise, which is interpreted as evidence of the time required for transfer of the initial uranyl excitation to a neptunyl site.

We created two kinetic decay models to explain the rise-time for the red waveform shown in Fig. 4: one assuming that energy was transferred by the radiative process and a second that included a term to represent RNET. The results of fitting these models to the data are shown in Fig. 5. The red trace is a model which includes only radiative energy transfer, the green trace includes RNET, and the black trace is the experimental data. It can be clearly seen that the RNET model is a better fit, giving a transfer rate of ~2.2×10^5 s^{-1} for crystals doped with 0.3% $Cs_2NpO_2Cl_4$. We were also able to estimate the efficiency of energy transfer to be greater than 90%.

The energy transfer rate can also be derived by measuring the lifetime of the $Cs_2UO_2Cl_4$ host crystal with and without the acceptor present. For the 0.3% doped crystal, a transfer rate of 2.5×10^5 s^{-1} was found using the lifetime of the host crystal, in agreement with that found using the model. Because the transfer is so efficient, we were able to detect $Cs_2NpO_2Cl_4$ at much smaller concentrations than we previously thought possible. To date, we have detected very strong neptunyl photoluminescence in crystals containing as little as 0.1% $Cs_2NpO_2Cl_4$. In fact, for the 0.1% doped crystals it was found that photoluminescence intensity was enhanced by a factor ~10 times over direct excitation of $Cs_2NpO_2Cl_4$ itself.

Summary

We have observed RNET between two different actinide ions in the solid state. The energy transfer process was modeled and found to be very fast and efficient in $Cs_2UO_2Cl_4$ crystals containing small quantities of $Cs_2NpO_2Cl_4$ (as low as 0.1%). This opens the possibility of using RNET to enhance photoluminescence from low quantum yield open-shell actinide molecules. We plan to synthesize crystals with lower concentrations of $Cs_2NpO_2Cl_4$—our current estimates suggest we could go as much as one order of magnitude lower in concentration and still detect emission from the dopant. We are currently analyzing the time-resolved photoluminescence data as a function of $Cs_2NpO_2Cl_4$ concentration to gain a more detailed understanding of the RNET process in the $Cs_2U(Np)O_2Cl_4$ system.

Further reading:

1. *M. M. Olken, C. M. Verschoor, and A. B. Ellis, "Host-to-guest, excited-state energy transfer in lamellar solids. Photoluminescent properties of hydrated europium uranyl phosphate", Inorg. Chem. 1986, 25, 80–82.*
2. *M. P. Wilkerson and J. M. Berg, "Excitation spectra of near-infrared photoluminescence from Np(VI) in $Cs_2U(Np)O_2Cl_4$", Radiochim Acta 2009, 97, 4–5, 223–226.*
3. *J. E. Bernard, D. E. Berry, and F. Williams, "Introduction to Energy Transfer and Relevant Solid-State Concepts" in Energy Transfer Processes in Condensed Matter, B. D. Bartolo and A. Karipidou, Ed., Plenum Press, New York, 1984, p1.*
4. *R. G. Denning, J. O. W. Norris, and D. Brown, "The electronic structure of actinyl ions. V. f-f transitions in $[NpO_2Cl_4]^=$ and $[NpO_2(NO_3)_3]^-$", Mol. Phys. 1982, 46, 287–323.*
5. *R. G. Denning, J. O. W. Norris, and D. Brown, "The electronic structure of actinyl ions. VI. Charge transfer transitions in $Cs_2NpO_2Cl_4$ and $CsNpO_2(NO_3)_3$", Mol. Phys. 1982, 46, 325–364.*

Radiation Damage in Plutonium from a Local Structure Perspective

The arrangement of atoms at the smallest scales, e.g. in a crystal lattice, is directly tied to many properties of interest, such as the strength of a bulk material. This relationship can be exploited with processing techniques to fine-tune performance, e.g., using heat treatments to make brittle forms of steel flexible. The connection between structure and properties becomes especially apparent as one considers the numerous changes brought about by radiation damage. In the high radiation environment of a nuclear power reactor, changes in thermal conductivity, creep, void swelling, radiation-assisted stress corrosion cracking, etc. all become issues that require monitoring the total dose and dose rate a material is exposed to. However, for materials such as plutonium in the nuclear stockpile, there is no "off switch" for radioactive decay. We therefore turn to measurements of the local structure using extended X-ray absorption fine structure (EXAFS) to gain a better understanding of the processes of radiation damage and aging mechanisms at work in plutonium.

For simplicity, we have focused on the predominant plutonium isotope, Pu-239. During the transmutation (decay) of Pu-239 into U-235 and He-4 (i.e., an alpha particle), in addition to changes in chemistry and composition that accompany each decay, 5.2 MeV of energy is released and carried away as kinetic energy of the daughter products (Eqn. 1). Most of this energy dissipates as heat. On a gram-for-gram basis, the amount of heat released by radioactive decay in plutonium is roughly equivalent to the chemical energy liberated by the same mass of high explosive every month. This striking fact not only shows the amazing amount of energy released by a miniscule fraction of the material decaying (Pu-239 has a half-life of 24,100 years), but highlights importance of the rate of that release.

(1) $$^{239}\mathrm{Pu} \xrightarrow{T_{1/2} = 24{,}110\ \mathrm{yrs}} {}^{235}\mathrm{U} + \alpha + 5.2\ \mathrm{MeV}$$

As damaging as the decay events are, they are spaced out far enough in time that the material does not blow itself to pieces in a matter of months. But changes to its structure, and consequently its properties, do occur, and for that reason a technical understanding of the nature of radiation damage in plutonium is of great importance as we seek to safely maintain our nuclear weapons stockpile without nuclear testing. Traditional methods of estimating radiation damage predict that each collision cascade from radioactive decay in plutonium creates approximately 2500 Frenkel (vacancy and interstitial) pairs (Fig. 1), suggesting that in a standard isotopic mixture of plutonium, every atom is displaced from its initial position in the crystal lattice once every 10 years. This extraordinary calculation illustrates the challenge that self-irradiation poses for these materials. This estimate of 0.1 dpa (displacement per atom) per year relies on several simplifications—one of the most significant being that it does not account for annealing of damage after the cascade event.

Mechanism of structural damage and annealing

Even below room temperature there is enough thermal energy in the material to start annealing vacancies and interstitials—in other words, the heat released from

Daniel T. Olive

Daniel Olive was a Seaborg Fellow from September 2015–August 2017. His area of interest was the study of radiation damage in plutonium, with mentor Alison Pugmire. He is now a staff member in the Materials Science and Technology Division, Nuclear Materials Science Group (MST-16).

«« *A* **Frenkel pair** *refers to a type of defect in a crystal structure in which an atom is displaced, creating a vacancy at the original site and an interstitial defect at the new location (Fig. 1).*

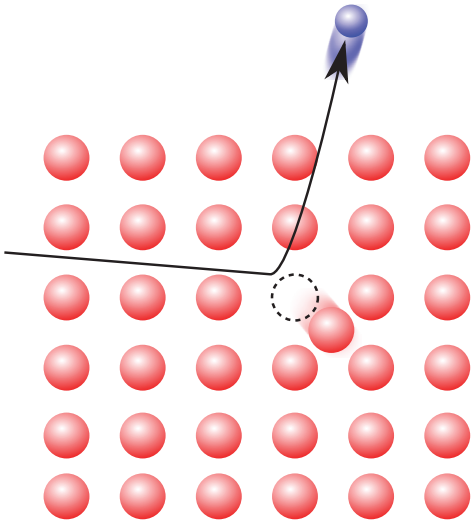

Figure 1. A fast-moving daughter product from alpha decay can knock atoms from their lattice positions, shown here creating a vacancy (dotted circle) and nearby interstitial pair. The energy released from a single alpha decay of plutonium is enough to create thousands of these defects.

»» *A* **Fourier transform** *is an important technique in physics which separates a complex signal into a series of constituent frequencies. For instance, a musical chord is composed of a set of constituent pitches (frequencies), and a Fourier transform could be used to identify them.*

the decay can work to fix the damage that it caused. Moments after the damage cascade disrupts the material, nearby vacancies and interstitials are likely the first to recombine. Subsequently, according to traditional theories for radiation damage in metals, there is enough energy for interstitials to become mobile, which begin to migrate until they find a vacancy, or another type of defect like a grain boundary to annihilate or recombine with. At higher temperatures there is enough energy to free trapped interstitials, and clusters start to form. Raising the temperature higher, vacancies likewise become mobile, then form clusters, loops, or other extended structures. Finally, at high enough temperatures, even these larger defect structures get annealed out, and the material returns to its undamaged state.

In order to study these annealing stages, a common approach is to cool the material close to liquid helium temperature, freezing all annealing processes, and then irradiate the sample to create damage. Measurements of physical properties, such as resistivity, which show change as a function of radiation damage, or EXAFS, which probes the local structure directly, can then be used to study the material in its most damaged state. The temperature of the sample can then be increased, and changes corresponding to each annealing stage become apparent. Fortunately, unlike most regular metals, plutonium does not require any special facility to perform these irradiation studies, as the ever-present alpha decay provides self-irradiation. However, due to the complicated behavior of 5f electrons in plutonium, it is unlike a regular metal in many of its other properties. For instance, pure plutonium can adopt six crystal structures before melting, the most of any element in the periodic table, and a more recent result from 2015 suggests that its ground state is governed by quantum fluctuations.

The ground state α-phase of pure plutonium is a brittle structure, which is difficult to manipulate and machine, therefore small amounts of gallium are typically added to obtain the more malleable δ-phase at room temperature (crystal structures shown in Fig. 2). Although the δ-phase has a face-centered cubic structure, typical of many metals, the gallium alloying process and the availability of other potential structures means we must take care in attempting to apply radiation damage models derived from regular metals to plutonium.

EXAFS overview

We turned to EXAFS to study radiation damage from the perspective of changes to the local structure for both plutonium and gallium in the material. These measurements show minute changes in the X-ray absorption of an element as a function of energy. By changing the energy of the incoming X-ray photon, the energy, and hence wavelength, of the photoelectron ejected after an absorption also changes. The outgoing wave scatters off of nearby atoms, like ripples from rocks in a pond. Constructive and destructive interference between these waves slightly alters the absorption probability, resulting in oscillations in the absorption spectrum. Changes in the distances of nearby atoms affect the frequency of the perturbation, and the number and disorder of the nearby atoms primarily affects the amplitude of the perturbations. By applying a Fourier transform to the EXAFS signal, the contributions of neighboring atoms become readily apparent, and detailed fitting of the measured spectrum to calculated spectra using the EXAFS equation allows one to extract structural information of the atoms near a particular element in a sample.

Studying structural changes in gallium-stabilized plutonium

Our research into radiation damage in plutonium has focused on two different areas. The first, dubbed "cold storage" involved keeping the sample at cryogenic

temperatures for a period of time, on the order of months. This effectively halted the annealing mechanisms, and allowed us to study the nascent damage state of the material, as described above. The other area of study involved examining damage that accumulates under ambient conditions. This was accomplished using EXAFS to measure the as-aged samples and counterparts that have been annealed above 420 K. Data from the latter method, dubbed "high temperature annealing", is more difficult to analyze as we are comparing changes in the structure that occur in the final annealing stages, which are necessarily larger in spatial extent, using information essentially averaged from all the atoms that the X-ray beam samples. Nevertheless, both of these techniques have revealed several important observations.

Cold storage

At low temperatures, the lattice can sustain an incredible amount of damage which can be annealed by warming for just a few minutes at room temperature. In a sample of plutonium containing 4.3 at.% gallium, after a few months of cold storage during which there was roughly one radioactive damage cascade for every 150,000 atoms, there was enough damage to the lattice that roughly half of the EXAFS signals from both the plutonium and gallium disappeared. This reduction is due to atomic disordering which disrupts the constructive interference effects that are relied upon in the EXAFS method. As the sample was warmed to successively higher temperatures before returning to cryogenic temperatures for measurements, the damage started to anneal. Most of the crystal structure (ca. 90%) returned to normal by 150 K, and the sample was restored to its original condition by the time it warmed to ambient temperature (300 K), within experimental error.

The gallium atoms show interesting differences from plutonium in their annealing behavior, particularly between 35 and 150 K. This is despite the substitutional character of the doped gallium, i.e., occupying the same positions as the plutonium atoms in the lattice. Although both gallium and plutonium sites experience a shrinkage of near-neighbor distances in the damaged state, the effect is more than twice as large in the gallium. Furthermore, the restoration of bond distances occurs at a lower temperature in the gallium atoms, closer to 35 K—the same temperature at which it appears to gain additional disorder, according to data fitting. Our interpretation is that immediately after the damage cascade, the gallium atoms tend to preserve their crystalline environment more effectively than plutonium, likely a product of their stabilizing capability in the lattice, and as the temperature warms and the annealing process starts they begin to take on a configuration more similar to the average structure of the damaged material. The plutonium atoms, in contrast, do not go through the additional disordering phase, and start a smooth path to recovery around 100 K.

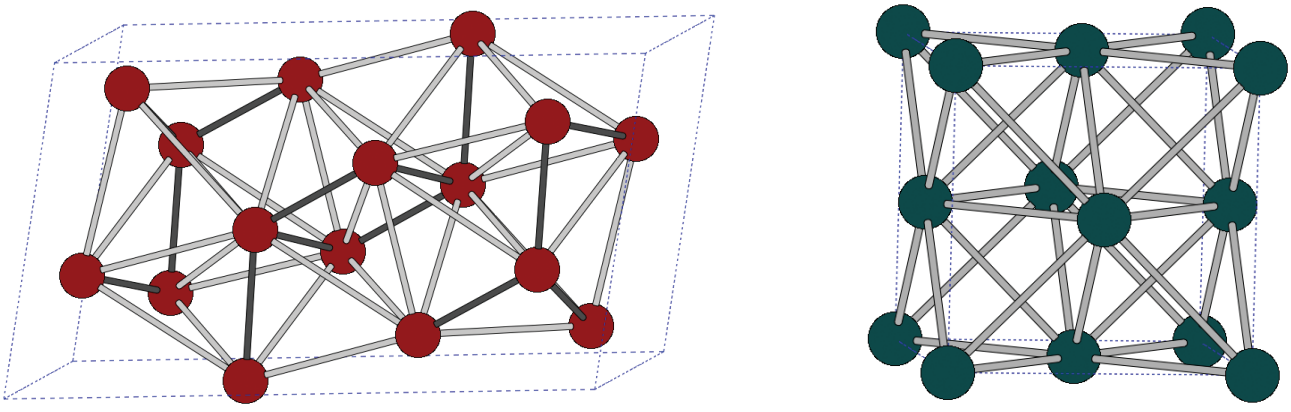

Figure 2. Unit cells of α-phase (left) and δ-phase (right) plutonium. The α-phase has 16 atoms in its unit cell, and each atom has between 12 and 16 bonds to its neighbors, roughly grouped into short (dark gray) and long (light gray) lengths. The δ-phase has 4 equivalent atoms per unit cell (for clarity, atoms shared with a neighboring unit cell are drawn whole), all with 12 equal length bonds.

Acknowledgments

Financial support for this work was provided by the U.S. Department of Energy through the LANL LDRD Program and the Glenn T. Seaborg Institute for Transactinium Science. The principal scientific aspects of this work are derived from a collaboration between LANL personnel (Daniel Olive, Alison Pugmire, and Franz Freibert) and Corwin Booth of Lawrence Berkeley National Laboratory. EXAFS data were acquired at the Stanford Synchrotron Radiation Lightsource, SLAC National Accelerator Laboratory, and was supported by the U.S. DOE, Office of Science, Office of Basic Energy Sciences under Contract No. DE-AC52-76SF00515.

High temperature annealing

Preliminary results studying ambient temperature damage in gallium-stabilized plutonium also show an interesting trend with respect to gallium concentration, as revealed in our high-temperature annealing experiments. These experiments involved studying samples ranging from 10 to 50 years old, which is enough time to accumulate measurable changes in structure that persist even after the majority of damage from each decay is annealed at ambient temperature. For these samples, a brief high-temperature anneal (above 420 K) is enough to remove this residual damage accumulation.

Looking at the effects of long-term aging using this process, we have observed that as the gallium concentration is increased, but remaining a small percentage of the material, there appears to be a reduction in accumulated damage as observed in the plutonium EXAFS data. Meanwhile, the gallium data from these samples indicates an increase in disorder around these atoms as their concentration increased. The sample set is still limited at present, and additional samples for comparison across a range of ages and gallium concentrations are still needed. However, these results highlight the importance of understanding the fundamental science of gallium as a stabilizer in the lattice and the numerous processes at work constantly creating and annealing damage in the material. This will be necessary if we are to truly understand and predict how the mechanical properties of Ga-stabilized Pu change with time.

Future work and summary

There are several important aspects to radiation damage in plutonium that we hope to resolve with continued work. Namely, we aim to shed more light on the variables that affect the radiation damage rate, such as gallium concentration or prior thermal history. Another goal is to better incorporate our work with larger scale models such as cluster dynamics, rate theory, or molecular dynamics, in order to improve predictions about the evolution of material properties with age. Finally, a deeper understanding of these complex changes will be gained by moving beyond the major constituents, plutonium and gallium, to the more difficult task of understanding the local environment of the relatively low-concentration uranium daughter products that grow into the material.

EXAFS has proved to be a remarkable tool for understanding the complicated radiation damage and annealing behavior in Pu. The ability to observe changes from the perspective of each element in the material has shed light on the stabilizing effect Ga has in the alloy δ-phase. Despite directly substituting Pu in the crystal lattice, Ga behaves differently in terms of its recovery from the damaged state, observed via cold storage experiments, and may serve an important role in reducing the amount of damage incorporated into the Pu lattice, as observed in the high temperature annealing experiments. These results, if combined with complementary experimental measurements of dynamic properties, have the potential to inform our fundamental understanding of radiation damage in plutonium and consequently improve our ability to make predictions about the storage behavior of this unusual material.

Further reading:

1. *D. T. Olive, D. L. Wang, C. H. Booth, E. D. Bauer, A. L. Pugmire, F. J. Freibert, S. K. McCall, M. A. Wall, and P. G. Allen, "Isochronal annealing effects on local structure, crystalline fraction, and undamaged region size of radiation damage in Ga-stabilized δ-Pu", J. Appl. Physics, 2016, 120, 3, 035103.*
2. *C. H. Booth and D. T. Olive, "Effect of temperature and radiation damage on the local atomic structure of metallic plutonium and related compounds", Adv. Phys., 2017, 10, 2, 1, 1–21.*
3. *C. H. Booth, Y. Jiang, S. A. Medling, D. L. Wang, A. L. Costello, D. S. Schwartz, J. N. Mitchell, P. H. Tobash, E. D. Bauer, S. K. McCall, M. A. Wall, and P. G. Allen, "Self-irradiation damage to the local structure of plutonium and plutonium intermetallics", J. Appl. Phys., 2013, 113, 093502.*
4. *M. Janoschek, P. Das, B. Chakrabarti, D. L. Abernathy, M. D. Lumsden, J. M. Lawrence, J. D. Thompson, G. H. Lander, J. N. Mitchell, S. Richmond, M. Ramos, F. Trouw, J.-X. Zhu, K. Haule, G. Kotliar, and E. D. Bauer, "The valence-fluctuating ground state of plutonium," Sci. Adv., 2015, 1, 6.*
5. *D. L. Clark, S. S. Hecker, G. D. Jarvinen, and M. P. Neu "Plutonium" in The Chemistry of the Actinide and Transactinide Elements, L. R. Morss, N. M. Edelstein, J. Fuger, and J. J. Katz, Eds., (Springer, 2008), Ch. 7.*
6. *W. G. Wolfer, "Radiation Effects in Plutonium," Los Alamos Science, 2000, 26, 274–285.*

G. T. Seaborg Institute Postdoctoral Fellows Program

The G. T. Seaborg Institute Postdoctoral Fellows Program supports research in heavy-element science relevant to Laboratory mission intersects with *nuclear energy*, *nuclear weapons*, and *global security* by attracting and funding a future generation of postdoctoral scientists.

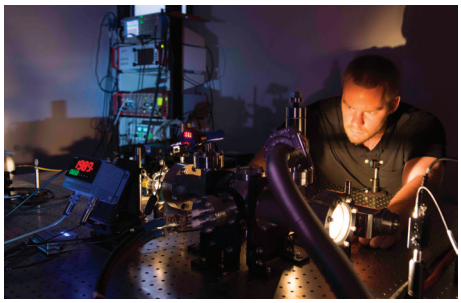

Nuclear Science Targets

Objectives for this project include materials, material properties, signatures, modeling, predictions, fabrication, detection, disposal, global security implications, forensics, and the specialized science surrounding actinides and especially plutonium, uranium, and their surrogates as fuels for energy and nuclear weapons.

Goal

Advancing nuclear science in a comprehensive project that ties targeted research with Los Alamos mission imperatives.

Mechanism

Research is supported from a multi-year broad-based postdoctoral fellows project. The Seaborg Institute works to maintain a balance among the many research areas. The program provides approximately half-time support and a modest amount of M&S funds. The appointments cover a two-year period.

Candidates

Successful applicants must be approved for division funding by the LANL postdoctoral program and be performing research in materials, material properties, signatures, modeling, predictions, fabrication, detection, disposal, global security implications, forensics, and the specialized science surrounding actinides and especially plutonium, uranium, and their surrogates as fuels for energy and nuclear weapons.

Oct. 1, 2018: Next call for applications (Oct. 29 deadline)

www.lanl.gov/projects/national-security-education-center/seaborg

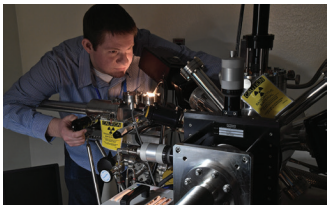

G. T. Seaborg Institute Summer Research Fellowships 2019

We are pleased to announce a nationwide search for 8-10 outstanding graduate student candidates to participate in the Seaborg Institute Summer Research Fellowships Program at Los Alamos National Laboratory, sponsored by the Department of Energy and the G. T. Seaborg Institute for Transactinium Science. Research Fellowships will be offered in two major areas:

Nuclear and Radiochemistry *nuclear forensics, homeland security, nuclear medicine, isotope production, nuclear physics, and related areas.*

Actinide Science *f-element chemistry and physics, spectroscopy, surface science, materials science, metallurgy, and related areas.*

Fellowships generally run 10-12 weeks and give students an opportunity to join Los Alamos scientists in independent research projects that can contribute to their thesis or advanced degree. While at Los Alamos, Research Fellows are encouraged to attend our weekly lecture series on a wide variety of current research topics presented by Los Alamos experts. Students are expected to present their research results at a poster session at the end of the summer experience.

Application Procedure

A complete application package will include a Fellowship Application, CV, two letters of recommendation, and current transcripts (official or unofficial).

Application forms can be found at *www.lanl.gov/projects/national-security-education-center/seaborg/summer-research*. Submit your application and supporting documents by email to seaborg@lanl.gov. Supporting documents (CV, letters of recommendation, etc.) may be submitted separately; please include the applicant name in the subject email when submitting supporting documents.

Eligibility

Students must be enrolled full-time at the time of application. Selection will be made on the basis of the applicant's academic record, recommendation letters, and research interests.

Salary

Students are paid a competitive salary based on Laboratory guidelines. Graduate student temporary employee salaries are based on the number of academic school years completed. More information can be found on LANL's education page at: *www.lanl.gov/careers/career-options/student-internships/graduate*.

Living Accommodations

Living accommodations and arrangements are the responsibility of the Research Fellow. Housing in Los Alamos is limited and summer housing options fill quickly. It is recommended that you begin researching housing options as soon as possible. LANL Housing Links can be found at *www.lanl.gov/careers/life-at-lab/northern-nm-living.php*. See also the Facebook page *Los Alamos County Rentals* (NM).

Sept. 24, 2018: Next call for applications (Oct. 29 deadline)

Actinide Research Quarterly is published by Los Alamos National Laboratory and is a publication of the Glenn T. Seaborg Institute for Transactinium Science, a part of the National Security Education Center. ARQ (est. 1994) highlights research in actinide science in such areas as process chemistry, metallurgy, surface and separation sciences, atomic and molecular sciences, actinide ceramics and nuclear fuels, characterization, spectroscopy, analysis, and manufacturing technologies.

LA-UR-18-27836

Address correspondence to:
Actinide Research Quarterly
c/o Editor
Mail Stop T-001
Los Alamos National Laboratory
Los Alamos, NM 87545

ARQ can be read online at:
www.lanl.gov/arq

If you have questions, comments, suggestions, or contributions, please contact the ARQ staff at:
arq@lanl.gov

National Security Education Center
David L. Clark, Director

G. T. Seaborg Institute for Transactinium Science
Science Advisors
Franz Freibert, Director (Acting)
Ping Yang, Deputy Director (Acting)

Editor
Owen Summerscales

Contributing editors
Susan Ramsay

Designers/Illustrators
Don Montoya
Owen Summerscales

Circulation Manager
Susan Ramsay

Los Alamos
NATIONAL LABORATORY
EST. 1943

NNSA